Developmental overproduction of cortical superficial neurons impairs adult auditory cortical processing

Mirna Merkler[1], Nancy Y Ip[2], Shuzo Sakata[1]✉

[1] Strathclyde Institute of Pharmacy and Biomedical Sciences, University of Strathclyde, 161 Cathedral Street, Glasgow G4 0RE, UK

[2] Division of Life Science, State Key Laboratory of Molecular Neuroscience and Molecular Neuroscience Center, The Hong Kong University of Science and Technology, Clear Water Bay, Kowloon, Hong Kong, China

✉Correspondence: shuzo.sakata@strath.ac.uk

Summary

While evolutionary cortical expansion is thought to underlie the evolution of human cognitive capabilities, developmental expansion can lead to megalencephaly, often found in neurodevelopmental disorders such as autism spectrum disorder. Still, little is known about how the overproduction of cortical neurons during development affects cortical processing and behavior in later life. Here we show that the overproduction of cortical superficial neurons leads to hyposensitivity to auditory stimuli in mice. We took advantage of a WNT/β-catenin signaling inhibitor, XAV939, to overproduce cortical superficial excitatory neurons during development. XAV939-treated adult mice exhibited a higher threshold to detect acoustic stimuli behaviorally. This behavioral deficit is associated with abnormal auditory cortical processing, such as higher delta power as well as lower spontaneous and auditory-evoked activity in putative excitatory cells. On the other hand, the auditory thalamus did not show any significant difference in neural firing between XAV939-treated and control groups. Within auditory cortical populations, functional monosynaptic connections were reduced across cell classes. A computational model predicts that the weakened excitatory-inhibitory connections lead to reduced spontaneous and evoked activity. Altogether, our results suggest that atypical auditory processing in XAV939-treated animals originates from weakened synaptic connections among cortical neurons. Although the expansion of cortical size is evolutionarily advantageous, an abnormal expansion during development can cause detrimental effects on cortical processing and perceptual behavior in adulthood.

Key words

auditory cortex, cortical layers, perceptual decision, neurodevelopmental disorders, autism spectrum disorder, Neuropixels

Introduction

The mammalian brain has evolved the neocortex with a prominent six-layered structure (Douglas and Martin, 2004, Szentagothai, 1983, Harris and Shepherd, 2015, Striedter, 1997, Gilbert, 1983). Over a hundred transcriptionally distinct neuron types can be identified across cortical laminae and they exhibit highly diverse functional properties (Yao et al., 2021, Harris et al., 2019, Gouwens et al., 2019, Kawaguchi and Kubota, 1997, Markram et al., 2004, Network, 2021, Sakata and Harris, 2009, Senzai et al., 2019, Hodge et al., 2019). Although we have witnessed tremendous progress on the characterization of neuronal diversity and circuit operations in the neocortex over the past decade, we still know little about to what extent the changes in the *number* of cortical neurons affects neural computation. As neuron number has long been considered a crucial factor for neural function (Williams and Herrup, 1988, Herculano-Houzel, 2009) and because the number of active neurons has been recognized as a fundamental feature to realize efficient neuronal processing (Barlow, 1972, Olshausen and Field, 2004, Barth and Poulet, 2012), it is important to address this issue experimentally.

The number of cortical neurons is primarily determined by two fundamental factors in development, that is, the length of the neurogenic period and the number of neurons generated per unit of time (Wilsch-Brauninger et al., 2016, Lewitus et al., 2014, Lui et al., 2011). Deficits in neural stem cell proliferation and differentiation can lead to neurodevelopmental disorders, such as autism spectrum disorder (ASD) and intellectual disability (Iakoucheva et al., 2019, Ernst, 2016). While a wide range of anatomical abnormalities has been associated with ASD, macrocephaly can be observed in ~15% of autistic patients (Fidler et al., 2000, Fombonne et al., 1999, Hazlett et al., 2017, Piven et al., 1995). However, it remains unclear how such abnormalities in cortical development can lead to abnormalities in cortical information processing and behaviors in later life.

Over the past decade, various mouse models of neurodevelopmental disorders have been developed (Kazdoba et al., 2016, Nestler and Hyman, 2010, Silverman et al., 2010). While some models reflect genetic deficits in human patients, environmental factors during development can also contribute to ASD (Kim et al., 2017, Choi et al., 2016). Yet, it is still challenging to manipulate developmental processes, especially the number of neurons, in a time-limited fashion. Here we take advantage of a WNT/β-catenin signaling inhibitor, XAV939 (Huang et al., 2009). This drug inhibits Tankyrase, which stimulates Axin degradation through the ubiquitin-proteasome pathway (Huang et al., 2009). Axin, a master scaffolding protein for cortical development (Fang et al., 2013, Ye et al., 2015), contains several functional domains to interact with signaling molecules including Tankyrase. Cytosolic Axin modulates various downstream signaling of extracellular signals, such as Wnt, Notch and TGFβ, whereas nuclear Axin regulates gene expression by interacting with β-catenin and other transcription factors. Mutations in the *Axin* gene are associated with abnormal brain size (Heisenberg et al., 2001, Kavaslar et al., 2000). Consistently, *in utero* microinjections of XAV939 in mice overproduce cortical superficial excitatory neurons and lead to autism-like behavioral phenotypes (Fang et al., 2014). This treatment does not alter the production of interneurons, microglia or astrocytes (Fang et al., 2014). However, it remains to be explored how the overproduction of cortical excitatory neurons can affect cortical processing at the neural circuit level.

Here, we address this issue by combining behavioral and *in vivo* large-scale electrophysiological recording approaches in the XAV939-treated mouse model. We particularly focus on their auditory function since ASD patients often exhibit abnormal sensitivity to acoustic stimuli (Robertson and Baron-Cohen, 2017, O'Connor, 2012). We report that XAV939-treated mice exhibit hyposensitivity to acoustic stimuli. This behavioral deficit is associated with abnormalities in auditory cortical activity, in terms of spontaneous and evoked population activity. We also report that weakened functional

synaptic connections across cortical neurons can explain this deficit.

Results

Overproduction of cortical superficial neurons by *in utero* XAV939 microinjections

To overproduce cortical superficial neurons, we injected XAV939 into the lateral ventricle of mouse embryos at embryonic day (E) 14.5, when intermediate progenitor cells that will differentiate into L2/3 excitatory neurons are proliferated (**Figure 1A**). To examine the effect of XAV939 microinjections, we performed histological analysis at postnatal day (P) 2 and 21 (**Figures 1B-D**). As reported previously (Fang et al., 2014), we confirmed that cortical superficial layers are significantly expanded in treated animals compared to vehicle controls at P2 ($n_{control}$ = 15 animals, $n_{treated}$ = 16 animals, $p < 0.05$, *t*-test) (**Figure 1C**) and P21 ($n_{control}$ = 13 animals, $n_{treated}$ = 13 animals, $p < 0.001$, *t*-test) (**Figure 1D**). Using this animal model, we investigated whether and how the developmental overproduction of cortical superficial neurons affects auditory processing in adults.

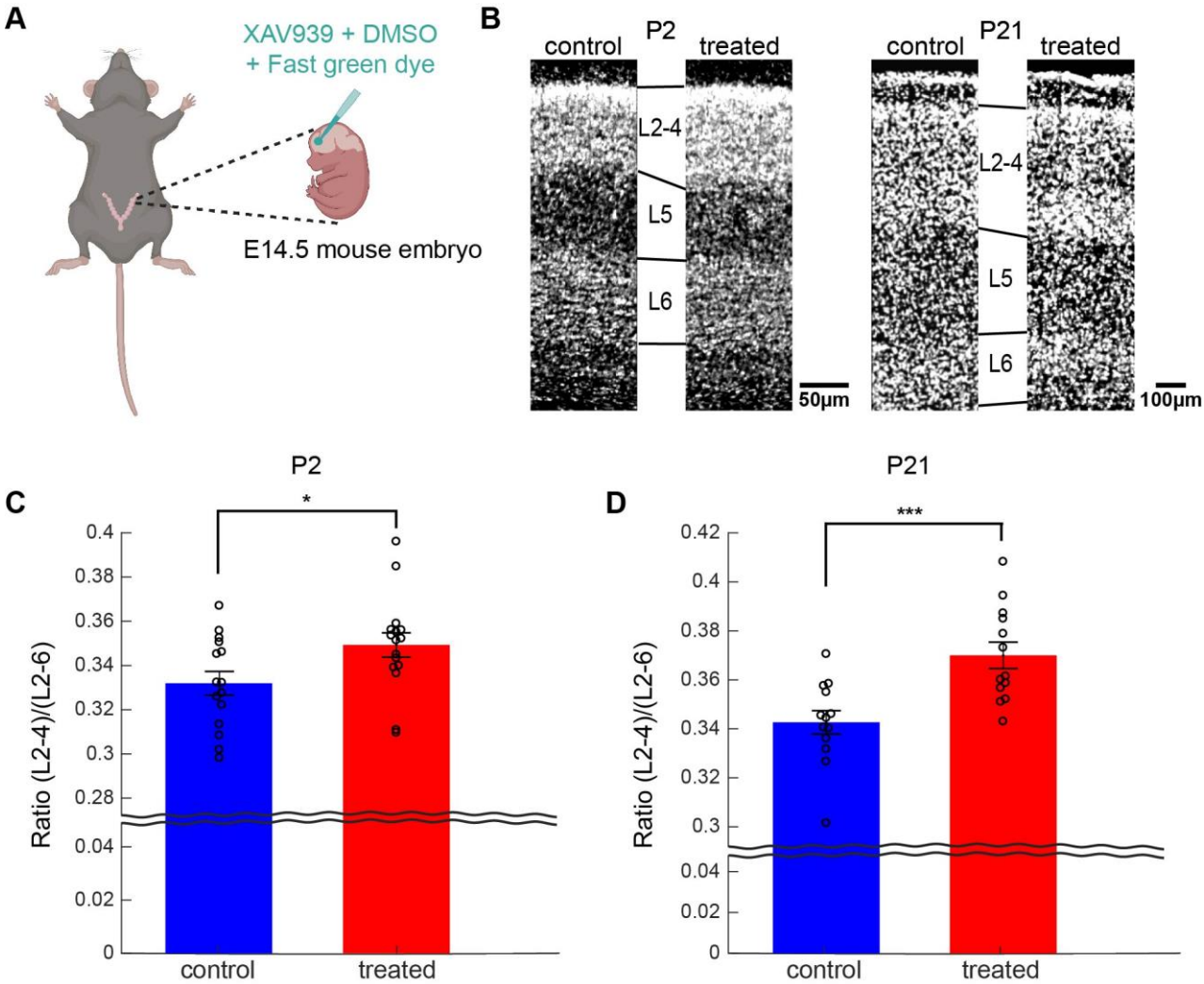

Figure 1 – XAV939 caused an increase in the width of cortical superficial layers.
(A) Schematics of *in utero* microinjections. Image was created with BioRender. **(B)** Comparison of cortical layer width between a control and a treated mouse on postnatal day 2 (P2; left) and P21 (right). **(C and D)** Fraction of cortical superficial layers (L2-4) at P2 **(C)** and P21 **(D)**. Error bars indicate SEM; *$p < 0.05$, ***$p < 0.001$; *t*-test (**C** and **D**).

Hyposensitivity to auditory stimulus in XAV939-treated adult mice

To examine the perceptual ability of XAV939-treated mice, we trained adult (~P70) mice to perform an auditory detection task in a head-restrained condition (**Figure 2**). In this task, mice were required to perform a licking response when they perceived a broadband white noise with varied intensities. When mice correctly detected a sound, they were rewarded with water. In a "catch" trial, no sound was presented. Although both treated and control animals reached the performance threshold (success rate ≥ 60%) without any notifiable differences, except reaction time (**Figure 2 – figure supplement 1**), we found a significant effect of treatment on detection performance, measured by *d'* ($n_{control}$ = 22 sessions, $n_{treated}$ = 32 sessions, $F_{1,53}$ = 4.11, p < 0.05, two-way ANOVA) (**Figure 2C**). We also estimated detection threshold by applying a logistic regression analysis (see Methods). We found a significantly higher detection threshold of XAV939-treated mice compared to that of control mice ($n_{control}$ = 22 sessions, $n_{treated}$ = 32 sessions, p < 0.05, rank sum test) (**Figure 2C** inset). Consistent with these observations, the effect of treatment on the average reaction time was also significant ($n_{control}$ = 22 sessions, $n_{treated}$ = 32 sessions, $F_{1,53}$ = 12.87, p < 0.0005, two-way ANOVA) (**Figure 2D**). Thus, the developmental overproduction of cortical superficial neurons led to a hyposensitivity to auditory stimulus in adult mice.

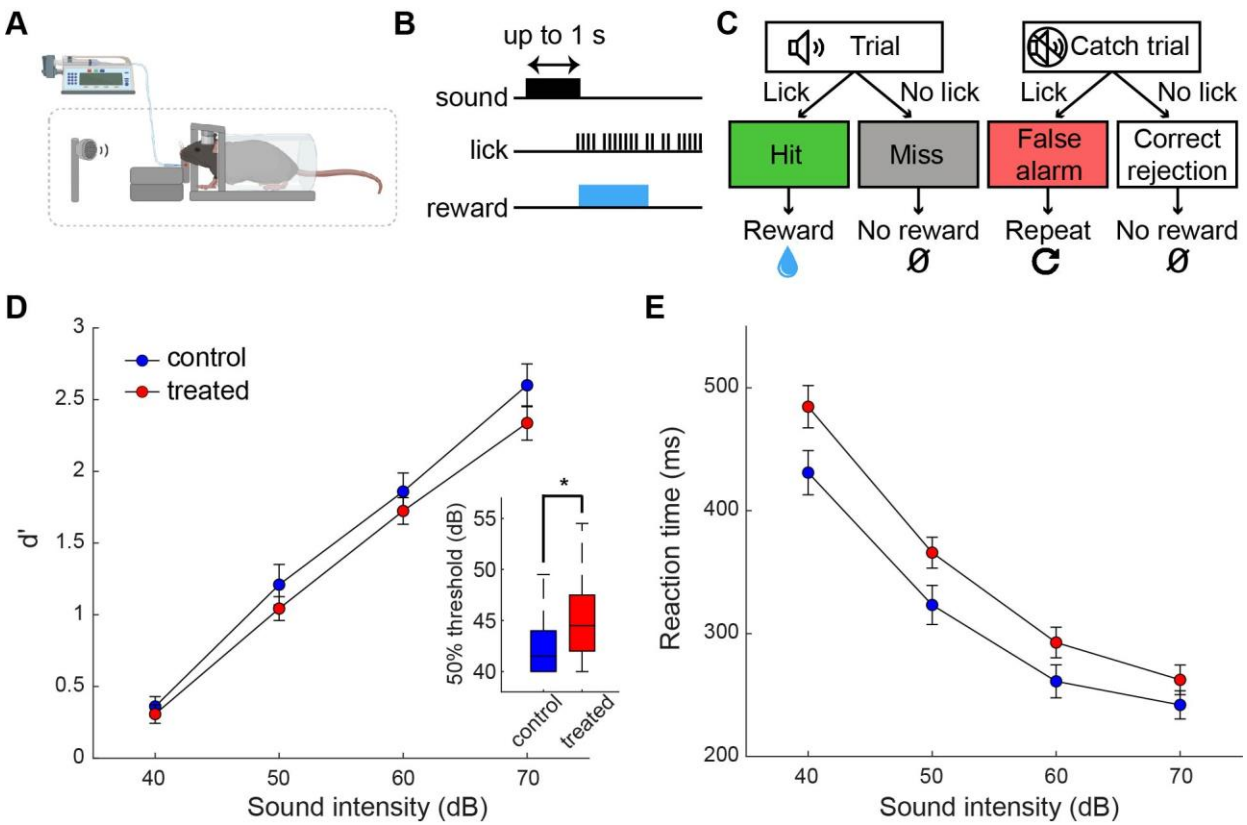

Figure 2 – XAV939 treated mice exhibit hearing deficits.
(A) Schematics of head-fixed behavioral training. Elements located inside a soundproof box are positioned within the dashed box. Image was created with BioRender. **(B)** Timeline of events in the auditory detection task. Trial starts with the sound onset. If the mouse licks during the response window (lasting 1 s), the sound turns off and water reward is delivered. **(C)** Diagram of possible events and outcomes during an auditory detection task session. **(D)** Comparison of *d'* between control and treated mice across sound intensities (n = 22 vs. 32 sessions; 2 sessions per mouse). Inset: Detection threshold comparison between control and treated mice. **(E)** Comparison of reaction time between control and treated mice across sound intensities (n = 22 vs. 32 sessions; 2 sessions per mouse). Error bars indicate SEM; *p < 0.05; Two-way ANOVA (**D** and **E**), rank sum test (**D** inset).

The following figure supplement is available for figure 2:

Figure supplement 1. Behavioral training progress and treatment effect in auditory conditioning.

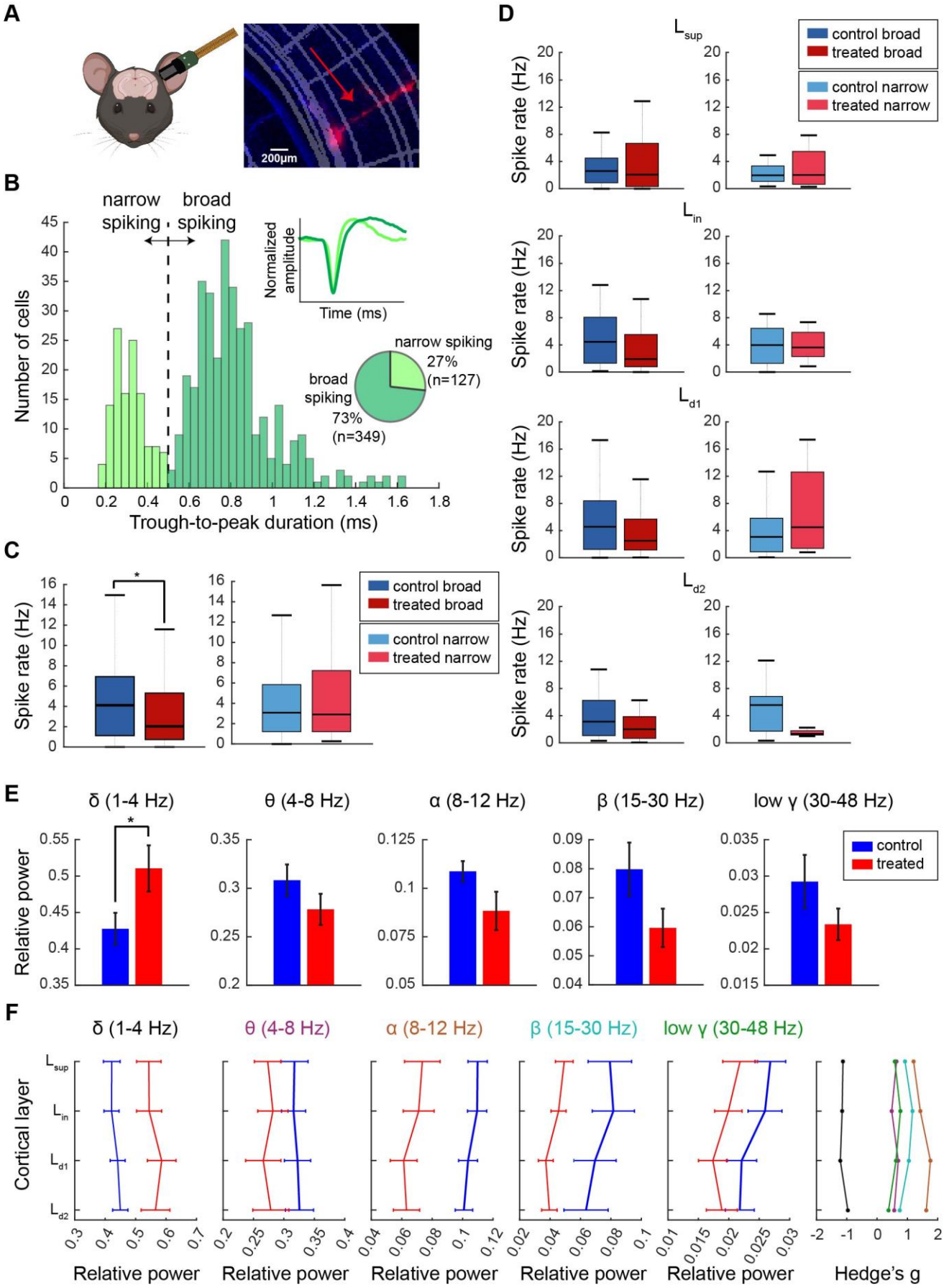

Figure 3 – Spontaneous cortical activity was significantly altered in treated mice.
(A) Schematics of Neuropixels probe insertion (left) and histological confirmation of the probe location in the auditory cortex (right). The schematics was created with BioRender. **(B)** Cell type classification depending on their waveform trough to peak duration. Two clusters (broad-spiking; BS and narrow-spiking; NS) were split at 0.5 ms border. Top inset: comparison between narrow and broad waveform. Bottom inset: Total number and percentages of BS and NS neurons across all recordings (passive listening and task performing), used in further analysis. **(C)** Spontaneous activity in control and treated mice (n = 141 vs. 134 BS cells, and 67 vs. 40 NS cells). **(D)** Spontaneous activity across cortical layers. L_{sup}, putative L2/3; L_{in}, putative L4; L_{d1}, putative L5; L_{d2}, putative L6. **(E)** Comparison of relative power across frequency bands in control and treated mice during silence. Power was calculated for one L_{sup} channel (located at the depth of 100 µm above the CSD sink channel) in each recording (n = 14 vs. 14 recordings). **(F)** Relative resting state power across cortical layers, for each frequency band (n = 8 vs. 9 recordings). Hedge's g was calculated to look at the effect of treatment for each cortical layer across frequency bands. Error bars indicate SEM; *p < 0.05; Rank sum test (**C** and **D**), t-test (**E**).
The following figure supplements are available for figure 3:
Figure supplement 1. Brain area estimation in Neuropixels recordings.
Figure supplement 2. Cortical cell depth determination with current source density analysis.
Figure supplement 3. Hippocampal relative power across frequency bands during silence.

Abnormal spontaneous population activity in XAV939-treated auditory cortex

To investigate the underlying neural mechanisms of the hyposensitivity to auditory stimulus, we performed *in vivo* electrophysiological recordings in both passive listening and task-performing conditions (**Figures 3-7**). We used either 64-channel silicon probes or Neuropixels probes to monitor population activity (**Figure 3A**): the latter probes allowed monitoring activity from both the auditory cortex and the auditory thalamus simultaneously. In the auditory cortex, we recorded from 216 neurons (174 from 9 passive listening animals across 17 recordings; 42 from 3 task-performing animals across 4 recordings) in treated animals and 260 neurons (208 from 8 passive listening animals across 15 recordings; 52 from 2 task-performing animals across 4 recordings) in control animals. In the auditory thalamus, we recorded from 147 neurons (82 from 4 passive listening animals across 6 recordings; 65 from 2 task-performing animals across 3 recordings) in treated animals and 54 neurons (13 from 1 passive listening animal across 2 recordings; 41 from 2 task-performing animals across 4 recordings) in control animals. We further classified cortical neurons into broad-spiking (BS; putative excitatory) neurons ($n_{control}$ = 184; $n_{treated}$ = 165) and narrow-spiking (NS; putative fast-spiking) neurons ($n_{control}$ = 76; $n_{treated}$ = 51) based on their spike waveforms (**Figure 3B**).

Analyzing these datasets, we firstly examined whether and how spontaneous activity in the auditory cortex was modified in XAV939-treated animals under a passive listening condition (**Figures 3C-F**). We found that the spontaneous firing rate of BS neurons was significantly lower in treated animals compared to that in control animals ($n_{control}$ = 141 cells, $n_{treated}$ = 134 cells, p < 0.05, rank sum test) (**Figure 3C, left**). On the other hand, spontaneous firing rate of NS neurons was not significantly affected by the treatment ($n_{control}$ = 67 cells, $n_{treated}$ = 40 cells, p = 0.62, rank sum test) (**Figure 3C, right**). Based on the depth profile of spike waveforms and current source density (CSD), we broke down auditory cortical neurons according to their depths (**Figure 3 – figure supplement 2**). While we observed varied modifications across layers, BS neurons in deep layers tended to exhibit a low, but not a significantly different, firing rate (L_{sup}, p = 0.68; L_{in}, p = 0.27; L_{d1}, p = 0.13; L_{d2}, p = 0.22, rank sum test) (**Figure 3D**). We also assessed spontaneous neural oscillations between groups based on local field potentials (LFPs) (**Figures 3E and F**), where delta (1-4 Hz) power was significantly enhanced in treated animals ($n_{control}$ = 14 recordings, $n_{treated}$ = 14 recordings, p < 0.05, t-test) (**Figures 3E and F**).

Although it was not statistically significant (p = 0.08), alpha (8-12 Hz) power tended to be reduced in treated animals. In **Figure 3F**, we also assessed LFP powers across cortical layers and frequency bands. The effect size (Hedge's g) was consistently low (~-1) and high (>1) across layers in the delta and alpha bands, respectively. By taking the advantage of Neuropixels probe recording, we also assessed simultaneously monitored LFPs in the hippocampus to examine if this difference might originate from other regions (**Figure 3 – figure supplement 3**). We did not find any significant differences in oscillatory powers across frequency bands between two animal groups (n_{control} = 2 recordings, n_{treated} = 8 recordings, p = 0.98, p = 0.89, p = 0.93, p = 0.81, p = 0.85; t-test). These results indicate that the overall spiking activity of BS neurons reduces, and cortical dynamics becomes slower in XAV939-treated animals.

Abnormal auditory-evoked activity in XAV939-treated auditory cortex

Because the behavioral detection threshold was significantly elevated in the treated mice (**Figure 2D**), we hypothesized that auditory evoked responses in the auditory cortex of the treated animals are diminished. To test this, we began by comparing auditory evoked responses in BS and NS cells in treated and control mice (**Figures 4A and B**). As the sound intensity increased, evoked responses became larger. However, we noticed that evoked responses of BS neurons in treated mice were consistently lower than those in control mice (**Figure 4A**). To confirm this quantitatively, we computed the mean spike rate in a 50 ms window from the stimulus onset across cells (**Figures 4C and D**). In BS cells, auditory-evoked responses were significantly reduced in treated animals at 50 dB (n_{control} = 141 cells, n_{treated} = 134 cells, p < 0.01, rank sum test with Bonferroni correction) and 60 dB (p < 0.05, rank sum test with Bonferroni correction) (**Figure 4C**). NS neurons in treated mice tended to exhibit slightly elevated auditory-evoked responses, but with no significance (n_{control} = 67 cells, n_{treated} = 40 cells, p > 0.2 across all intensities, rank sum test with Bonferroni correction) (**Figure 4D)**.

We further assessed the laminar specificity in firing rate changes (**Figures 4E and F**). Evoked responses tended to be lower except in L_{sup}, with significant reduction in L_{d2} BS neurons (n_{control} = 23 cells, n_{treated} = 22 cells, p < 0.01 at 50 and 60 dB, p < 0.05 at 70 dB, rank sum test with Bonferroni correction). On the other hand, NS cells exhibited diverse effects (**Figure 4F**). Overall, XAV939-treatment led to a reduction in auditory evoked responses in BS neurons, especially in deep layers.

Abnormal auditory cortical activity in task-performing XAV939-treated mice

Next, we directly compared auditory cortical activity in task-performing animals between the two groups (**Figure 5A**). We confirmed lower baseline spontaneous activity in BS neurons in XAV939-treated mice (n_{control} = 43, n_{treated} = 31, p < 0.05, rank sum test) (**Figure 5B, left**). Auditory evoked responses in BS neurons were lower in treated mice (n_{control} = 43, n_{treated} = 31, p < 0.01 at 40 dB, p < 0.05 at 50 dB, rank sum test with Bonferroni correction) (**Figures 5C and E**). On the other hand, we did not find any significant differences in spontaneous (n_{control} = 9, n_{treated} = 11, p = 0.40, rank sum test) (**Figure 5B, right**) and auditory evoked activity (**Figures 5D and F**) in NS neurons (n_{control} = 9, n_{treated} = 11, p > 0.4 across all intensities, rank sum test with Bonferroni correction). Thus, the reduction in both spontaneous and auditory evoked activity in XAV939-treated mice was consistent between both passive listening and task-performing conditions.

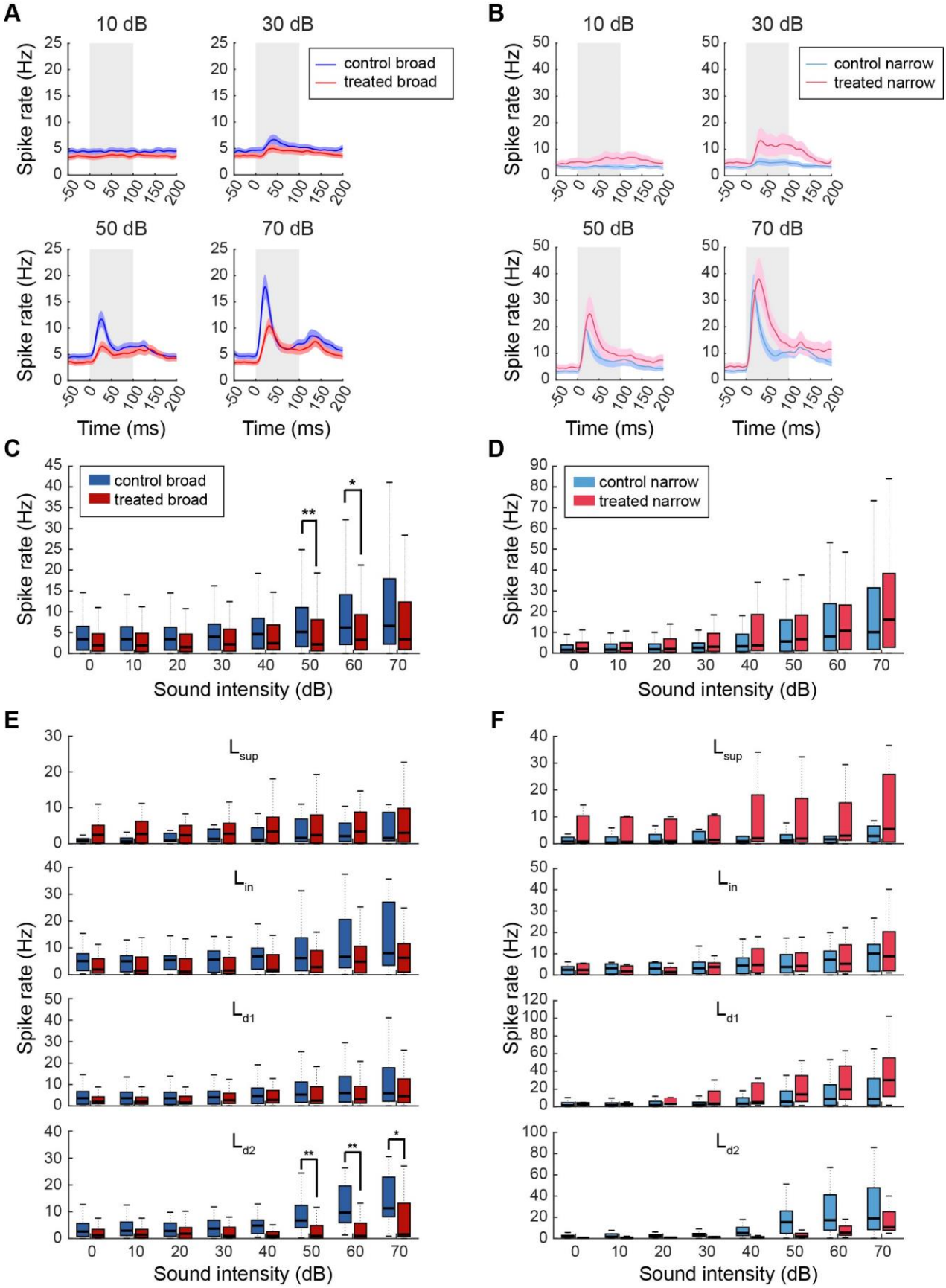

Figure 4 – Auditory evoked activity was affected by XAV939 treatment.

(A and B) Peristimulus time histogram (PSTH) of activity (mean ± SEM) of BS neurons **(A)** and NS neurons **(B)** in control and treated group during sound presentation. Sound period is labelled as a gray background (lasting 100ms). **(C and D)** Spike rate of BS **(C)** and NS **(D)** neurons during first 50 ms of

sound presentation. **(E and F)** Activity of cells shown in **(C)** and **(D)** split into cortical layers. *$p < 0.05$, **$p < 0.01$; Rank sum test with Bonferroni correction (**C – F**).

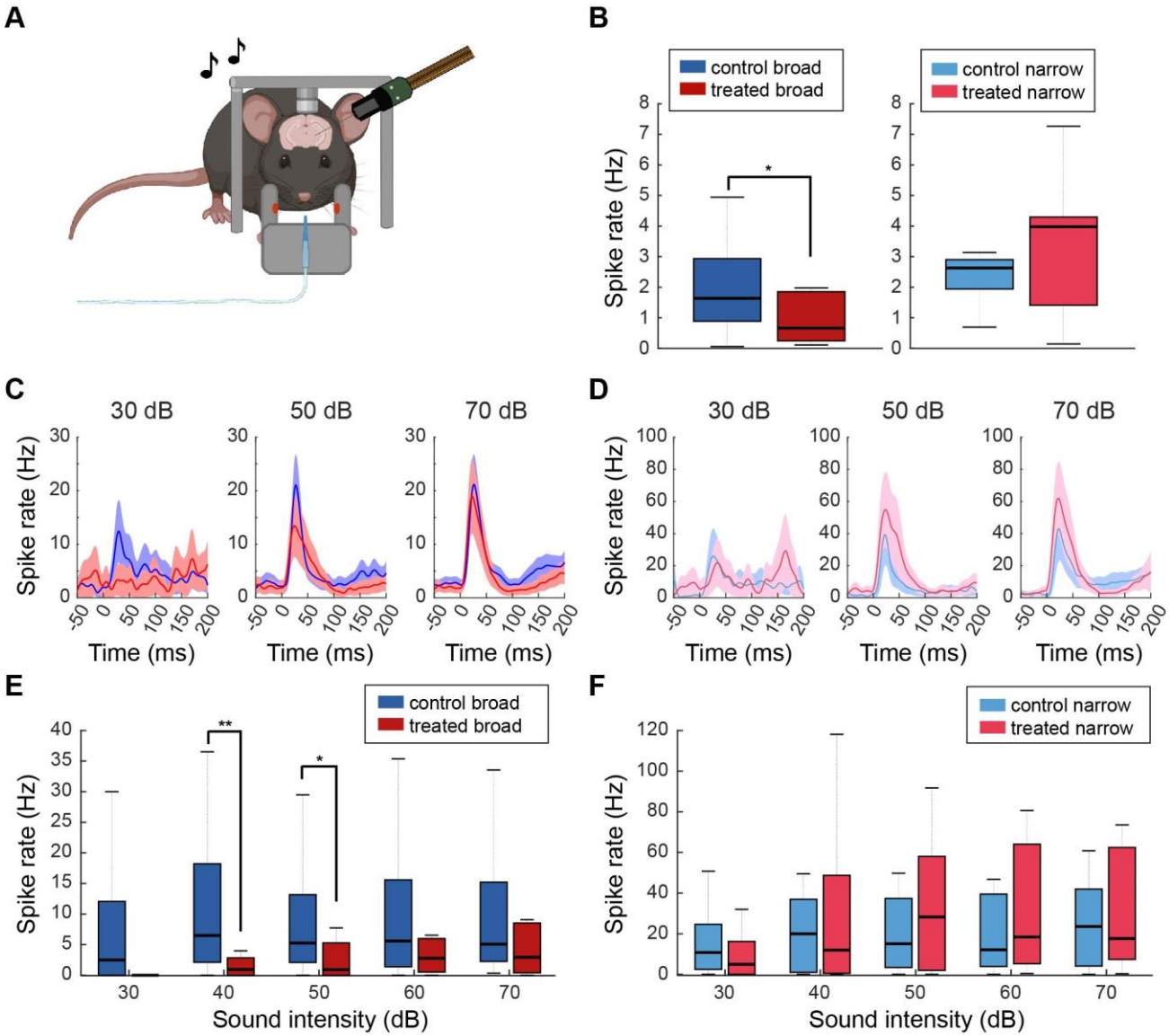

Figure 5 – Reduction in BS neuronal activity was observed in task behaving treated mice.
(A) Schematics of Neuropixels recording in task behaving head-fixed conditions. Image was created with BioRender. **(B)** Spontaneous activity during prestimulus window (1 s before trial onset), regardless of the trial type (n = 43 vs. 31 BS cells, and 9 vs. 11 NS cells). **(C and D)** PSTH of average BS **(C)** and NS **(D)** activity (mean ± SEM) in control and treated group during sound presentation in trials with "hit" outcome. Sound onset is at 0 ms. **(E and F)** Activity of BS **(E)** and NS **(F)** neurons in trials with "hit" outcome, during first 50 ms from sound onset. Error bars indicate SEM; *$p < 0.05$, **$p < 0.01$; Rank sum test (**B**), rank sum test with Bonferroni correction (**E** and **F**).

Auditory thalamic activity in XAV939-treated mice

To examine whether the observed abnormal activity in the auditory cortex of XAV939-treated animals is inherited from an upstream structure, we analyzed activity in the auditory thalamus (**Figure 6**). Neurons were recorded from multiple auditory thalamic nuclei, not just the ventral division of the medial geniculate body (MGBv) (**Figure 6 – figure supplement 2**). We found that MGB neurons did not show any significant differences in spontaneous ($n_{control}$ = 13, $n_{treated}$ = 82, p = 0.74, rank sum test) (**Figure 6B**) or auditory evoked activity between two animal

groups ($n_{control}$ = 13, $n_{treated}$ = 82, p > 0.5 across all intensities, rank sum test with Bonferroni correction) (**Figure 6C**). These results imply cortical mechanisms for the hypofunction of auditory processing in XAV939-treated mice.

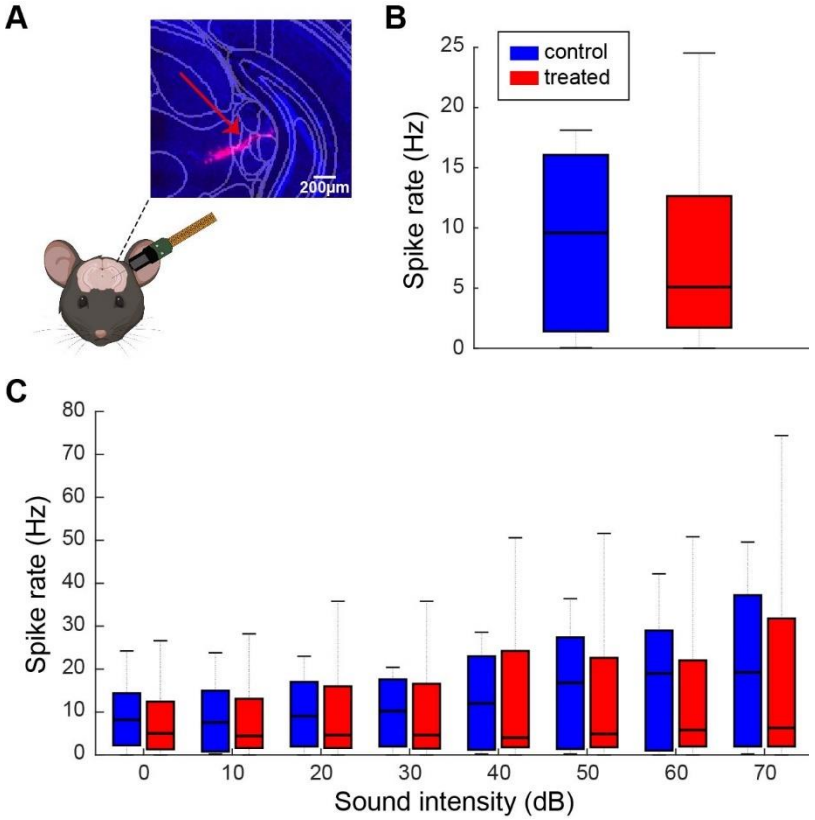

Figure 6 – Auditory thalamic activity was not affected by XAV939 treatment.

(A) Schematics of simultaneous Neuropixels recording from auditory cortex (AC) and medial geniculate body (MGB), with histological confirmation of probe location in MGB. **(B)** Spontaneous activity in MGB during passive listening conditions (n = 13 vs. 82 cells). **(C)** MGB activity in passive listening conditions across sound intensities. None were statistically significant (p > 0.05); Rank sum test **(B)**, rank sum test with Bonferroni correction **(C)**.

The following figure supplement is available for figure 6:

Figure supplement 1. Locating MGB in Neuropixels recordings.

Figure supplement 2. Auditory evoked activity across MGB nuclei.

Reduced effective connectivity in XAV939-treated auditory cortex

To explore a potential mechanism to explain abnormal auditory cortical processing in XAV939-treated animals, we inferred monosynaptic connections among simultaneously recorded neurons by computing cross-correlograms (CCGs) (**Figures 7A-D**). This approach allows us to identify strong synaptic coupling between neurons based on their spike trains (Fujisawa et al., 2008). As shown in **Figure 7A**, there are three types. Firstly, if there is no strong coupling, no significant modulation can be seen. On the other hand, if there are strong effective connections from one neuron to another, significant excitatory or inhibitory modulations can be seen within several milliseconds after spikes. We systematically assessed these effective couplings across all simultaneously recorded neurons in the auditory cortex (**Figures 7B-D**). Across datasets, such connections were generally sparse in both groups (**Figure 7B**). However, when we compared the connection probability of individual neurons between two animal groups, we found significantly lower connection probabilities of the following connections in XAV939-treated mice: from BS to BS ($n_{control}$ = 147, $n_{treated}$ = 150, p < 0.01, rank sum test with Bonferroni correction), from BS to NS ($n_{control}$ = 147, $n_{treated}$ = 150, p < 0.001, rank sum test with Bonferroni correction) (**Figure 7C**), and from NS to NS ($n_{control}$ = 70, $n_{treated}$ = 44, p < 0.05, rank sum test with Bonferroni correction) (**Figure 7D**). These results suggest weakened cortical synaptic connections in XAV939-treated mice.

Weakened synaptic connectivity explains reduced spontaneous and evoked activity

To investigate whether these weakened synaptic connections between excitatory and inhibitory populations can explain the reduced cortical activity in XAV939-treated mice, we performed a simulation based on the Wilson-Cowan model, a population rate model (Wilson and Cowan, 1972) (see Methods) (**Figure 7E**). More specifically, we examined how different connection strengths between excitatory and inhibitory populations can influence their activity while the ratios of the connection probabilities were taken from the empirical results above and maintained across simulations. We solved differential equations numerically and found that the model in both conditions exhibited a steady state regardless of their initial condition (**Figure 7F**). We found that the steady state of the excitatory population was lower in the model based on the connectivity of XAV939-treated mice (**Figure 7F**). We also simulated evoked responses by providing extrinsic signals transiently. We observed that transient evoked responses of the excitatory population were lower in the model based on the connectivity of XAV939-treated mice (**Figure 7F**).

We further examined if the lower steady state can be seen even when the synaptic weights are changed systematically while maintaining the ratio across the connections (**Figure 7G**). We found that the steady state of the excitatory population is consistently lower in the model based on the connectivity of XAV939-treated mice (**Figure 7G**). These results suggest that the weakened synaptic connections between excitatory and inhibitory populations can explain the reduced activity in excitatory cortical populations of XAV939-treated mice.

Discussion

We examined how manipulating the number of cortical neurons during development affects cortical processing in adulthood. We found that XAV939-treated mice exhibit a reduction in behavioral performance during the auditory detection task, as well as having reduced spontaneous and auditory evoked activity in BS neurons of the auditory cortex. In addition, the functional monosynaptic connections between BS and NS neurons were weakened, and this explained the atypical auditory cortical processing. On the other hand, the auditory thalamus did not exhibit abnormal activity in XAV939-treated mice. Altogether, these results indicate that developmental overproduction of cortical superficial excitatory neurons leads to the hypofunction of auditory processing due to weakened cortical synaptic connections.

To the best of our knowledge, our study is the first to investigate how manipulating the number of cortical neurons affects cortical processing across layers and auditory perceptual behavior. Although XAV939 has been used to increase cortical superficial neurons previously, effects of XAV939 microinjections on adult behaviors are varied (Fang et al., 2014, Fang and Yuste, 2017): XAV939-treated mice exhibited autistic behaviors, such as repetitive behaviors and social deficits (Fang et al., 2014), and their visual discrimination ability was enhanced (Fang and Yuste, 2017). Unexpectedly, we observed a reduced detection ability in the auditory system. This contradiction can be explained by several factors. Firstly, it is possible that different modalities may exhibit distinct effects. Secondly, the overproduction of cortical superficial neurons may lead to distinct impacts on perceptual detection and discrimination. Because superficial excitatory populations encode sensory information sparsely (de Kock et al., 2007, Crochet et al., 2011, Sakata and Harris, 2009), the overproduction of superficial excitatory neurons may increase a coding space, leading to a better discrimination ability whereas this may not be the case for perceptual detection. Indeed, some visual domain clinical ASD studies report decreased signal detection ability while others report enhanced discrimination of simple stimuli (Bertone et al., 2005, Sanchez-Marin and Padilla-Medina, 2008). In addition, this apparent contradiction may be analogous to the fact that ASD patients often exhibit superior performance for details of their perceptual world, but this comes at a cost for the global perceptive (Robertson and Baron-Cohen, 2017, Shah and Frith, 1983). Future studies need to reconcile this discrepancy.

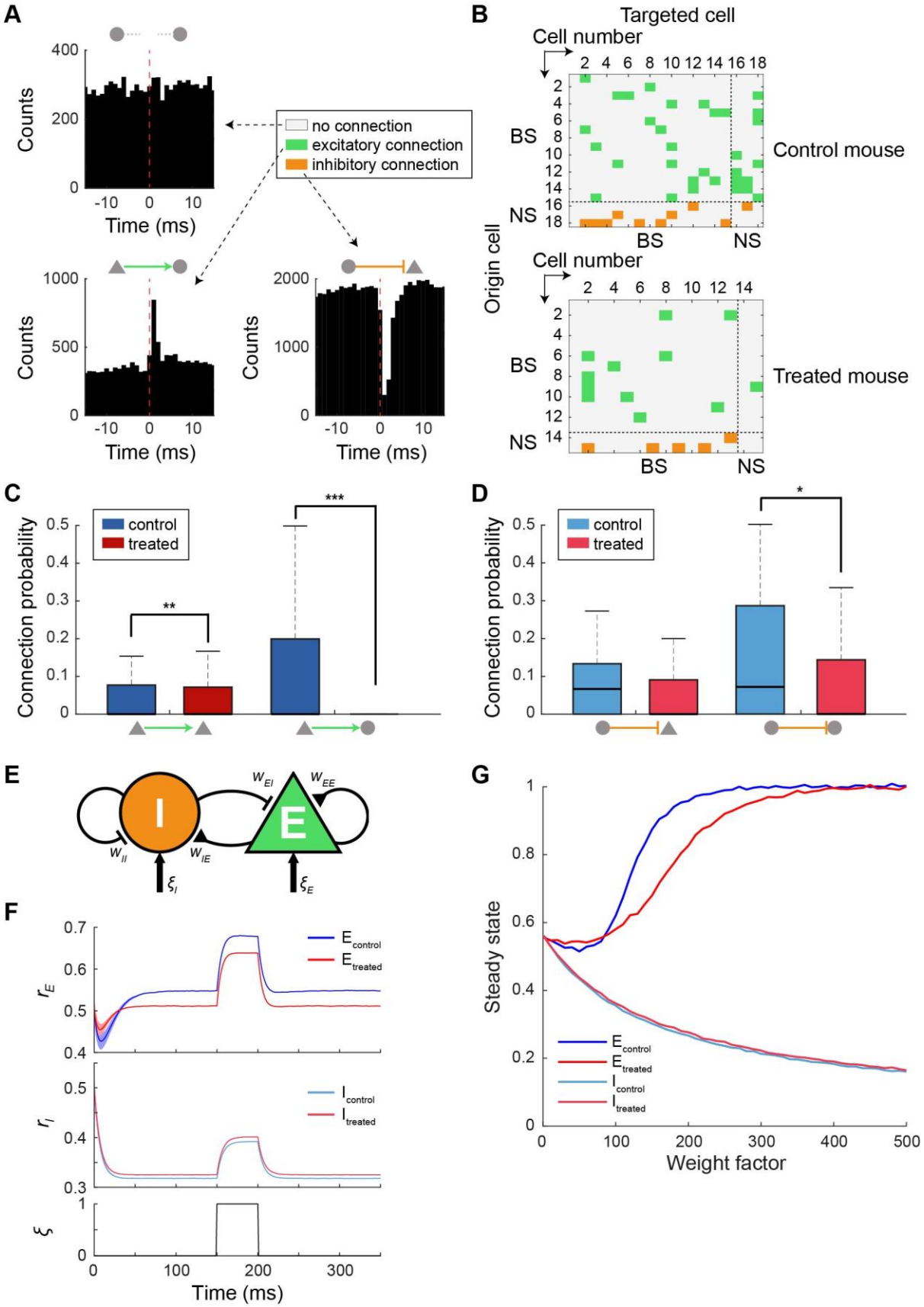

Figure 7 – XAV939 treated mice have fewer monosynaptic connections within the auditory cortex. (A) Examples of cross-correlograms between neuron pairs; neurons that are not connected (top), excitatory connection (bottom left) and inhibitory connection (bottom right). Red dotted line marks the spike time of origin cell, while histogram shows the activity of targeted cell. **(B)** Connectivity matrices from

one control and one treated mouse, showing the connections between simultaneously recorded neuron pairs. **(C)** Probability of an excitatory connection coming from BS neurons (triangle; n = 147 vs. 150) to either BS (triangle) or NS neurons (circle). **(D)** Probability of an inhibitory connection coming from NS neurons (circle; n = 70 vs. 44). **(E)** A schematic of the Wilson-Cowan model. Excitatory (E) and inhibitory (I) populations are mutually connected. Each population also has a self excitatory or inhibitory connection, respectively, with receiving an extrinsic input ξ. Connection strength is denoted as W. **(F)** Time domain analysis of the model. The initial condition of each population was varied systematically (from 0 to 1, 0.1 resolution). The weight factor was set as 100. At 150 – 200 ms, both populations received an extrintic input as 1. Data indicates mean ± SEM. **(G)** The steady state of each population in each condition is shown as a function of the weight factor. The steady state was determined as firing rate at 200 ms without any extrinsic input. *p < 0.05, **p < 0.01, ***p < 0.001; Rank sum test with Bonferroni correction (**C** and **D**).

Why did the overproduction of superficial excitatory neurons diminish the overall cortical activity? We hypothesize that mechanisms have emerged to compensate for the enhanced excitability in cortical circuits during postnatal development. It is consistent with the previous finding that XAV939 administration shifts the balance between excitatory and inhibitory synapses (Fang et al., 2014): the ratio of excitatory to inhibitory synapses in L2/3 in XAV939-treated animals increased at P18, whereas it decreased at P60. This change was associated with a reduction in field excitatory postsynaptic potentials, which is consistent with the present results. Thus, the excitation-inhibition balance may be changed over a period of time in the XAV939 model. In our results, we have observed a slight tendency of increase in putative inhibitory activity (**Figures 3C, 3D, 4B, 4D, 4F, 5B, 5D, 5F**), but not a significant one. During postnatal development, programmed cell death plays a prominent role in establishing appropriate numbers of excitatory and inhibitory cortical neurons (Verney et al., 2000, Southwell et al., 2012). Moreover, accumulating evidence has also demonstrated postnatal activity-dependent processes which sculpt cortical circuits (Thion et al., 2019, Wong et al., 2018). Thus, the overproduction of cortical superficial excitatory neurons during the prenatal period can trigger various compensatory mechanisms, resulting in reduced cortical excitability in adults.

Although the expansion of cortical size is advantageous on the evolutionary timescale (Herculano-Houzel, 2009), our results are consistent with the notion that abnormal expansion of cortical layers during development can lead to an imbalance of excitation and inhibition in the cortical network, resulting in detrimental effects, which can be seen in various neurodevelopmental disorders (Tang et al., 2021, Nelson and Valakh, 2015, Marin, 2012). Indeed, increased cortical volume and L2 neuron number have been reported in ASD (Falcone et al., 2021, Courchesne et al., 2011, Hazlett et al., 2017), and some ASD patients experience hypofunction of sensory systems (Robertson and Baron-Cohen, 2017). Our results suggest that altered cortical connections lead to such hypofunction. Our model (**Figure 7**) predicts a restoration of synaptic connections as a potential therapeutic strategy for ASD.

In conclusion, the overproduction of cortical superficial excitatory neurons during development weakens synaptic connections across cortical populations in adulthood. These altered synaptic connections lead to decreased spontaneous and evoked population activity as well as a higher behavioral threshold to detect auditory signals.

Acknowledgements

This work was supported by the BBSRC (BB/M009050X/1) and Horizon2020-RIA (DEEPER, 101016787) to SS, and the Area of Excellence Scheme of the University Grants Committee (AoE/M-604/16) to NYI. We would like to thank Lucy Morton for proof reading and Moataz Badawi for comments on the manuscript.

Author contributions

MM and SS designed and conceived the project and analyzed the data. MM performed all experiments. SS performed all simulations and supervised MM. NYI provided technical support for in utero microinjections. MM and SS wrote the manuscript with input from NYI.

Ethics statement

All animal experiments and procedures were performed in accordance with the United Kingdom Animals (Scientific Procedures) Act of 1986 Home Office regulations and approved by the Home Office (PPL70/8883 and PP0688944) and the University of Strathclyde's Ethical Committee.

Methods

Animal maintenance and XAV939 administration

Pregnant female wild-type C57BL/6 mice (*n* = 29) were housed in a 12 h light/dark cycle. *In utero* microinjections were performed on embryonic day 14.5 (E14.5), where embryos were injected with 0.15 or 0.4 µl of 10 µM XAV939 (X3004, Sigma Aldrich) in DMSO solution with 0.05% Fast Green dye (F7258, Sigma Aldrich; treated litter) or DMSO with 0.05% Fast Green dye solution (control litter), in the lateral ventricle. Mice were perfused on postnatal day 2 (P2) (*n* = 31) and P21 (*n* = 35) for histological assessment of cortical layers width. Only male mice were kept until adulthood (perfused ~P120) and used for behavioral (*n* = 30) and electrophysiological (*n* = 27) assessments.

Surgical procedure for experiments in head-fixed condition

The procedure was done as described elsewhere (Lyngholm and Sakata, 2019, Yague et al., 2017). Briefly, ~8 week old male mice were anesthetized with isoflurane (1 – 1.5%). To provide analgesia, Lidocaine (2%, 0.1 ml) was administered subcutaneously at the site of the incision and Carprofen (Rimadyl, 10 ml/kg, 0.01% diluted in water for injection) was administered subcutaneously in the back. Five screws (418-7123, RS Components) were implanted in the skull, two in the front (AP +1.5 mm, ML ±1.5 mm), two on the cerebellum (AP -6 mm, ML ±2 mm) and one over the right hemisphere (AP -3 mm, ML 3 mm). The posterior left screw was used as a ground, while the anterior right screw was used for cortical electroencephalogram (EEG) recording. The other screws were implanted for anchoring and stabilization of the head cap. A head-post made of 2 nuts was affixed onto the two frontal skull screws. During this surgery, the location of the future craniotomy site above the left hemisphere was also labelled (2 x 2 mm^2 at AP -2 mm and ML 4 mm). Dental cement was used to cover the skull screws and surface as well as to secure the head-post in place. After the surgery, mice were single housed in high-roofed cages with ad libitum access to food and water and left to recover for at least 5 days.

Behavioral experiments

Apparatus. A custom-made behavioral apparatus was located in a soundproof box (Med Associates Inc). A head-fixed mouse was placed in a restraining tube, with a spout, made from a pipette tip, in front of his mouth. The tip of the spout was aligned with a sensor (PMU24, Panasonic). The spout was connected by tubing to a 10 ml syringe filled with water and secured in a single-syringe infusion pump (AL-1000, World Precision Instruments). The pump was located outside of the box. To present the sounds, a calibrated speaker (ES1, Tucker-Davis Technologies) was placed ~15 cm in front of the mouse. Water delivery, sound presentation and sensor information were relayed through NI-DAQ (USB-6343, National Instruments) and controlled by a custom-written LabVIEW program (National Instruments). Broadband white noise was generated digitally (USB-6343, National Instruments) and amplified (System 3 ED1, Tucker-Davis Technologies) before being transmitted to the speaker.

Behavioral training. After recovery from surgical procedure, mice were placed into the reverse light/dark cycle and water restriction was

initiated a week after the adaptation to the new cycle. The restriction was daily, starting gradually until reaching 0.04 ml/g/day. During the restriction acclimation period of 7 days, mice were also habituated to handling and head fixation. Daily training sessions lasted 1 hr, during which mice received water through a water pump as a reward (1 - 3 µl water drop per pump). Mice were weighed after each session and the remainder of their daily water amount was delivered in the form of hydrogel (70-01-5022, ClearH2O). Behavioral training consisted of 3 phases: basic lick training, auditory conditioning and auditory detection.

In the first training phase (Basic lick training), mice were familiarized with the system. Whenever the mouse licked the spout, their tongue would cross the beam of the sensor activating the pump and water would be delivered. After making more than 300 licks in a session, the animal would move on to the next phase.

In the second phase (Auditory conditioning), mice were trained to lick only when a broadband white noise (60 dB SPL) was present. At first, the sound was presented for 8 s, followed by 2 s of silence. Mice could get a water reward only if they licked during the sound period. After 50 valid trials, the sound would be reduced by 1 s and silence increased by 1 s. The sound presentation was reduced in this way across sessions until reaching 2 s. If an animal had ≥ 150 licks with ≥ 60% success rate for 2 s sound periods in 2 consecutive sessions, they could move on to the final phase.

In the final phase (Auditory detection task), mice were trained and then later assessed in licking whenever they heard a sound, across different intensities. A broadband white noise (30 – 70 dB SPL, 10 dB SPL steps) was presented for a maximum of 1 s. Intertrial interval (ITI) in this phase lasted 2 – 4 s, and both intensities and ITI length were pseudo-randomized across trials. Catch trials were also present in this phase, allowing us to assess how often the mouse engaged randomly. When the difference between the catch trial false alarm rate and 70 dB hit rate was more than 40% in two consecutive sessions, after at least 10 training sessions, the mouse would finish training. These two sessions were used in analysis of behavioral performance.

In vivo electrophysiology

Detailed recording procedures have been previously described (Lyngholm and Sakata, 2019, Yague et al., 2017). One day before the recording, mice were briefly anesthetized with isoflurane and a craniotomy was done over the auditory cortex (AC) (see above for the coordinate), on the site marked previously during the head cap surgery. Craniotomy site was covered with a biocompatible sealant (Kwik-Sil, World Precision Instruments). During the recording sessions, Kwik-Sil was removed and phosphate buffer saline (PBS) was used to prevent the brain surface from drying. Neural population activity was recorded in ~1 hr daily sessions over 2 days. Head-fixed, awake mice were sat in a restraining tube within a soundproof box (Industrial Acoustics Company). Electrophysiological recordings were done with either a 64-channel silicon probe (A4x16-6mm-50-200-177-A64, NeuroNexus Technologies; recorded from AC) or with a Neuropixels 1.0 probe (recorded from AC and MGB), mounted on a micromanipulator (SM-15 or DMA-1511, Narishige). Probes were inserted perpendicular to the cortical surface (AC recording depth 750-900 µm; MGB recording depth ~4000 µm). Signals collected through the silicon probe were amplified and digitized (RHD2132 and RHD2000, Intan Technologies Inc.) and recorded using a custom-written LabVIEW program (National Instruments). Signals collected through the Neuropixels probe were amplified and digitized in the probes integrated circuit and recorded using SpikeGLX (Janelia Research Campus). The recording sessions were typically initiated ~30 min after the probe insertion, to allow for signal stabilization. Probes were labelled with either DiI (D-282, Invitrogen, 10% diluted in ethanol) or CM-DiI (C7001, Invitrogen, 0.1% w/v diluted in ethanol) before insertion, thus allowing us to find the probe track later in histology.

Sound presentation and behavioral task during electrophysiological recording. For passive listening experiments, broadband white noise (100-200 repetitions of 100 ms pulses with 1 ms cosine ramps, 10 dB SPL steps, 0-70 dB SPL intensity range presented pseudo-randomly, 500 ms interstimulus interval, ISI), was generated digitally (sampling rate 97.7 kHz, RZ6 Multi I/O processor, Tucker-Davis Technologies) and transmitted in free-field through a calibrated speaker (ES1, Tucker-Davis Technologies). In behavioral task recordings, broadband white noise was presented for a maximum of 1 s (or until the animal licking), in 30 – 70dB SPL range with 10 dB SPL steps, and 2 – 4 s ISI. Sound intensity and ISI were presented pseudo-randomly. Behavioral recording sessions lasted 1 hr. A water pump (AL-1000, World Precision Instruments) and sound presentation were controlled by a custom-written LabVIEW program (National Instruments). Licking sensor (PMU24, Panasonic) information was relayed through NI-DAQ (NI PCI-6221, National Instruments).

Histological analysis

Mice were injected intraperitoneally with a mixture of pentobarbital and lidocaine and perfused transcardially with PBS followed by 4% paraformaldehyde (PFA) in 0.1M PBS. Brain tissue was removed and stored in the same fixative overnight at 4°C, then transferred into 30% sucrose solution for at least 2 days. The tissue was cut into 80 µm coronal sections using a microtome (SM2010R, Leica), stained with DAPI, and observed under an epifluorescent upright microscope (Eclipse E600, Nikon). In adult mouse brain slices, post electrophysiological recordings, DiI/CM-DiI signals were also observed to evaluate the probe track.

Data analysis

Histological evaluation of superficial cortical layers. Width of cortical layers in P2 and P21 mice was measured using Fiji ImageJ on DAPI images taken with 4x magnification. Portion of superficial layers in the cortex was calculated using the formula: $W_{L2\text{-}4}/W_{L2\text{-}6}$, where $W_{L2\text{-}4}$ and $W_{L2\text{-}6}$ were the width of L2-4 and L2-6, respectively. Measurements of 3 adjacent areas were taken on each brain slice, one brain slice per mouse, and the mean of their ratios was compared to other brain slices. All measurements were done blindly to the treatment and grouped afterwards. In P2 mice, the measurements were taken in the frontal, somatosensory area, while at P21 the measurements were taken in the auditory cortical area.

Behavioral data. In each session, mean reaction time and detectability index (d') were calculated for all sound intensities. d' was calculated using the formula: $d' = Z(\text{hit rate}) - Z(\text{false alarm rate})$, where Z is the inverse of the standard normal cumulative distribution function. The detection threshold of each training session was estimated based on cross-validated logistic regression analysis. A logistic binomial model of the probability of hit as a function of sound intensity was created using MATLAB *fitglm* function. The detection threshold was defined as the sound intensity which reaches 50% hit. This process was repeated with a randomly chosen half of trials and the remaining half, and the threshold was calculated as the mean of them.

Electrophysiological recordings. All electrophysiological data analysis was performed offline. Spike sorting was performed with Kilosort or Kilosort2 (https://github.com/MouseLand/Kilosort), followed by manual curation with phy or phy2 (https://github.com/cortex-lab/phy). Quality of each cluster was assessed by their Mahalanobis (isolation) distance (Schmitzer-Torbert et al., 2005). For the firing rate comparison in passive listening conditions and all monosynaptic connection assessments, we included only the single units with an isolation distance ≥ 20 and an overall spike rate >0.1 Hz. For the activity comparison in task performing mice, we included all clusters with an isolation distance ≥ 20 and an overall spike rate >0.1 Hz. Cortical cells were further classified based on their spike waveforms (Lyngholm and Sakata, 2019, Yague et al., 2017). We set the threshold of the trough-to-

peak duration to 0.5 ms to distinguish between BS and NS cells.

Probe track estimation. To estimate which channels belong to which brain region in Neuropixels recordings, we assessed the overall multi-unit activity on each probe channel and cross-compared it with a 3D histological evaluation of the probe's trajectory made by SHARP-Track (https://github.com/cortex-lab/allenCCF/tree/master/SHARP-Track (Shamash et al., 2018)). Combining SHARP-Track information with known brain-area specific activity allowed us to determine which recording channels were located in the auditory cortex and which were in the thalamus (**Figure 3 – Figure supplement 1**). SHARP-Track borders are not exact, they are affected by tissue distortion and tearing during slice fixation. On average, the median absolute deviation between our electrophysiological and histological borders was 76 µm, which is comparable with a previous report (Steinmetz et al., 2019).

To define the MGB borders, we took the following two-step estimation approach (**Figure 6 – Figure supplement 1)**: (1) the estimation of the number of channels within MGB based on histological analysis, (2) the refinement of the channel positions based on auditory evoked responses. More specifically, by taking the output of the SHARP-Track analysis described above, we estimated the length of MGB passed by the Neuropixels probe. This length was converted to a corresponding number of electrode channels based on the spacing between electrodes. Secondly, we determined the latency of auditory evoked responses across all thalamic channels. For each channel, cell activity was split into 1 ms bins, filtered using 5 ms Gaussian kernel and normalized by evoked response threshold (2.8 SD from baseline mean, taken from 100 ms before the sound onset across trials). Therefore, all values above 1 were considered a significantly evoked response and latency was determined as the first occurrence of such response. Since most MGB neurons have a short latency of auditory stimuli (Anderson and Linden, 2011), we identified a cluster of channels exhibiting short response latency (<20 ms), and refined the MGB channel positions while maintaining the number of channels estimated by the first step.

Cortical laminar estimation based on current source density (CSD) analysis. In silicon probe recordings, signals from each channel were lowpass filtered (800 Hz), downsampled (1 kHz) and spatially smoothed across one top and one bottom neighboring channel. Neuropixels probe LFP signals were lowpass filtered (100 Hz), downsampled (1 kHz) and spatially smoothed across ±5 channels. Event-related potentials (ERP) were then calculated and filtered using lowpass and highpass Butterworth filter, and CSD was calculated using the formula: CSD = $((Va+Vb)-2Vo)/d^2$, where Vo is the observed channel, Va and Vb are its neighboring channels and d is the distance between channels (mm). CSD sink channel was set as the top border of input layer (L_{in}), which was then counted as depth 0, while the borders of deep layer 1 (L_{d1}; putative L5) and deep layer 2 (L_{d2}; putative L6) were determined based on layer thickness from previous publications (Cooke et al., 2018, Ji et al., 2016). Thus, L_{d1} top border was set at –150 µm and L_{d2} top border at –400 µm. Everything above 0 µm was considered as superficial layers (L_{sup}; putative L2/3). Out of 10 passive listening Neuropixels recordings, 4 recordings (1 from control and 3 from treated mice) were excluded from further laminar and LFP analysis due to excessive noise levels in LFP channels.

Spontaneous activity analysis. In passive listening mice, the spontaneous firing rate of each cell was calculated during a 5 min silent period recorded immediately after the noise presentation period. In the same silent period, Welch's power spectral density was calculated for five frequency bands (delta [1-4 Hz], theta [4-8 Hz], alpha [8-12 Hz], beta [15-30 Hz] and low gamma [30-48 Hz]) for each channel. Signals from the silicon probes were first extracted with a lowpass filter (800 Hz) and then downsampled to 1 kHz. Only the channels from one (middle) shank were taken into further analysis. For Neuropixels recordings, only one row of channels was used in LFP analysis. LFP signals were lowpass filtered (50 Hz) and spatially smoothed across ±2 channels before power spectral density calculation. For estimation of

mean power per cortical layer, only the recordings containing channels in all cortical layers were included. CSD results were used to split the channels into layers, and the mean relative power per layer was calculated for each recording. For L_{sup} mean power estimation, one channel located 100 µm above CSD sink was identified per recording and used in group comparisons. In task-performing mice, spontaneous activity was estimated from 1 s periods before the sound onset.

Auditory evoked neuronal activity. For PSTH, average activity during noise presentation of different intensities was calculated in every 1 ms bin across stimulus conditions. For statistical analysis of evoked neuronal activity, spike counts during the 50 ms time window from the sound onset were used.

Cross-correlation analysis. Monosynaptic connections assessment was done as described elsewhere (Fujisawa et al., 2008). After computing the original cross-correlograms (CCGs), 1000 surrogate CCGs were created to assess statistical significance. To create each surrogate CCG, spikes were randomly jittered ±3 ms and a CCG was calculated as a surrogate. Based on these surrogate CCGs, upper and lower bounds of confidence limit (1%; $p = 0.01$) were determined. When the original CCG values passed the confidence limit within the [-3:0 ms, 0:3 ms] time window, the interaction between cells was considered significant ($p < 0.01$). If the values passed the upper confidence limit, the interaction between neurons was considered as excitatory. Otherwise, if the values passed the lower confidence limit, the interaction was labelled as inhibitory.

Computational model

Abnormal cortical activity in XAV939-treated mice was simulated using a population firing rate model based on the Wilson-Cowan model (Wilson and Cowan, 1972). The model is comprised of mutually connected excitatory *E* and inhibitory *I* populations with self-excitatory and -inhibitory connections. The dynamics of *E* and *I* populations are governed by the following differential equations

$$\tau_E \dot{E}(t) = -E(t) + \sigma(w_{EE}E(t) - w_{EI}I(t) + \xi_E) + \eta,$$

$$\tau_I \dot{I}(t) = -I(t) + \sigma(w_{IE}E(t) - w_{II}I(t) + \xi_I) + \eta,$$

where *E(t)* and *I(t)* denote the level of activity in each neural population at a given time point. ξ_E and ξ_I denote the external input in each neural population. The synaptic weight *w* was proportional to that estimated from cross-correlation analysis described above, namely, $w_{EE} \sim 0.0532$, $w_{IE} \sim 0.0973$, $w_{II} \sim 0.145$, and $w_{EI} \sim 0.0795$ in the control condition, and $w_{EE} \sim 0.0314$, $w_{IE} \sim 0.0373$, $w_{II} \sim 0.0821$, and $w_{EI} \sim 0.0465$ in the treated condition. While maintaining the ratio, each *w* was scaled by the weight factor *g* to determine what range of weights can recapitulate experimental observations. Time constants were set to $\tau_E = 9$ ms and $\tau_I = 18$ ms, respectively. η denotes a random Gaussian noise where SD was set to 0.1. $\sigma(x)$ denotes the activation function of each neural population. It was defined as a sigmoid

$$\sigma(x) = \frac{1}{1+\exp(-\alpha x)},$$

where α determined the slope of the activation function and was set to 0.5. To simulate the dynamics of the model for 350 ms, the initial condition *E(0)* and *I(0)* were set to the range of values, from 0 to 1, and the time resolution of simulations was set to 0.01 ms. To evaluate spontaneous activity, we numerically determined the steady state of each neural population. To evaluate evoked response, ξ_E and ξ_I were increased to 1 in 150-200 ms. We examined a range of weight factor *g* from 0 to 500.

Statistical analysis

All statistical analysis was done using MATLAB. The effect was considered significant at $p < 0.05$. In Figures 1C, 1D, 3E, 2-S1A, 2-S1B, 2-S1C, 2-S1D and 3-S2 two sample *t*-test was performed. In Figures 2D and 2E a two-way ANOVA was performed. Rank sum test was done in Figures 2D (inset), 3C, 3D, 5B and 6B. Rank sum test with Bonferroni correction was performed in Figures 4C, 4D, 4E, 4F, 5E, 5F, 6C, 7C, 7D, 6-S1B and 6-S1C. To estimate effect size, Hedge's

g was calculated in Figure 3F, using a MATLAB toolbox (Hentschke and Stuttgen, 2011).

References

Anderson, L. A. & Linden, J. F. 2011. Physiological differences between histologically defined subdivisions in the mouse auditory thalamus. *Hear Res,* 274**,** 48-60.

Barlow, H. B. 1972. Single units and sensation: a neuron doctrine for perceptual psychology? *Perception,* 1**,** 371-94.

Barth, A. L. & Poulet, J. F. 2012. Experimental evidence for sparse firing in the neocortex. *Trends Neurosci,* 35**,** 345-55.

Bertone, A. M., L., Jelenic, P. & Faubert, J. 2005. Enhanced and diminished visuo-spatial information processing in autism depends on stimulus complexity. *Brain,* 128**,** 2430-41.

Choi, G. B., Yim, Y. S., Wong, H., Kim, S., Kim, H., Kim, S. V., Hoeffer, C. A., Littman, D. R. & Huh, J. R. 2016. The maternal interleukin-17a pathway in mice promotes autism-like phenotypes in offspring. *Science,* 351**,** 933-9.

Cooke, J. E., King, A. J., Willmore, B. D. B. & Schnupp, J. W. H. 2018. Contrast gain control in mouse auditory cortex. *J Neurophysiol,* 120**,** 1872-1884.

Courchesne, E., Mouton, P. R., Calhoun, M. E., Semendeferi, K., Ahrens-Barbeau, C., Hallet, M. J., Carter Barnes, C. & Pierce, K. 2011. Neuron number and size in prefrontal cortex of children with autism. *JAMA,* 306**,** 2001-10.

Crochet, S., Poulet, J. F., Kremer, Y. & Petersen, C. C. 2011. Synaptic mechanisms underlying sparse coding of active touch. *Neuron,* 69**,** 1160-75.

de Kock, C. P., Bruno, R. M., Spors, H. & Sakmann, B. 2007. Layer- and cell-type-specific suprathreshold stimulus representation in rat primary somatosensory cortex. *J Physiol,* 581**,** 139-54.

Douglas, R. J. & Martin, K. A. 2004. Neuronal circuits of the neocortex. *Annu Rev Neurosci,* 27**,** 419-51.

Ernst, C. 2016. Proliferation and Differentiation Deficits are a Major Convergence Point for Neurodevelopmental Disorders. *Trends Neurosci,* 39**,** 290-299.

Falcone, C., Mevises, N., Hong, T., Dufour, B., Chen, X., Noctor, S. C. & Cerdeño, V. M. 2021. Neuronal and glial cell number is altered in a cortical layer-specific manner in autism. *Autism,* 25**,** 2238-2253.

Fang, W. Q., Chen, W. W., Fu, A. K. & Ip, N. Y. 2013. Axin directs the amplification and differentiation of intermediate progenitors in the developing cerebral cortex. *Neuron,* 79**,** 665-79.

Fang, W. Q., Chen, W. W., Jiang, L., Liu, K., Yung, W. H., Fu, A. K. Y. & Ip, N. Y. 2014. Overproduction of upper-layer neurons in the neocortex leads to autism-like features in mice. *Cell Rep,* 9**,** 1635-1643.

Fang, W. Q. & Yuste, R. 2017. Overproduction of Neurons Is Correlated with Enhanced Cortical Ensembles and Increased Perceptual Discrimination. *Cell Rep,* 21**,** 381-392.

Fidler, D. J., Bailey, J. N. & Smalley, S. L. 2000. Macrocephaly in autism and other pervasive developmental disorders. *Dev Med Child Neurol,* 42**,** 737-40.

Fombonne, E., Roge, B., Claverie, J., Courty, S. & Fremolle, J. 1999. Microcephaly and macrocephaly in autism. *J Autism Dev Disord,* 29**,** 113-9.

Fujisawa, S., Amarasingham, A., Harrison, M. T. & Buzsaki, G. 2008. Behavior-dependent short-term assembly dynamics in the medial prefrontal cortex. *Nat Neurosci,* 11**,** 823-33.

Gilbert, C. D. 1983. Microcircuitry of the visual cortex. *Annu Rev Neurosci,* 6**,** 217-47.

Gouwens, N. W., Sorensen, S. A., Berg, J., Lee, C., Jarsky, T., Ting, J., Sunkin, S. M., Feng, D., Anastassiou, C. A., Barkan, E., Bickley, K., Blesie, N., Braun, T., Brouner, K., Budzillo, A., Caldejon, S., Casper, T., Castelli, D., Chong, P., Crichton, K., Cuhaciyan, C., Daigle, T. L., Dalley, R., Dee, N., Desta, T., Ding, S. L., Dingman, S., Doperalski, A., Dotson, N., Egdorf, T., Fisher, M., de Frates, R. A., Garren, E., Garwood, M., Gary, A.,

Gaudreault, N., Godfrey, K., Gorham, M., Gu, H., Habel, C., Hadley, K., Harrington, J., Harris, J. A., Henry, A., Hill, D., Josephsen, S., Kebede, S., Kim, L., Kroll, M., Lee, B., Lemon, T., Link, K. E., Liu, X., Long, B., Mann, R., McGraw, M., Mihalas, S., Mukora, A., Murphy, G. J., Ng, L., Ngo, K., Nguyen, T. N., Nicovich, P. R., Oldre, A., Park, D., Parry, S., Perkins, J., Potekhina, L., Reid, D., Robertson, M., Sandman, D., Schroedter, M., Slaughterbeck, C., Soler-Llavina, G., Sulc, J., Szafer, A., Tasic, B., Taskin, N., Teeter, C., Thatra, N., Tung, H., Wakeman, W., Williams, G., Young, R., Zhou, Z., Farrell, C., Peng, H., Hawrylycz, M. J., Lein, E., Ng, L., Arkhipov, A., Bernard, A., Phillips, J. W., Zeng, H. & Koch, C. 2019. Classification of electrophysiological and morphological neuron types in the mouse visual cortex. *Nat Neurosci,* 22**,** 1182-1195.

Harris, J. A., Mihalas, S., Hirokawa, K. E., Whitesell, J. D., Choi, H., Bernard, A., Bohn, P., Caldejon, S., Casal, L., Cho, A., Feiner, A., Feng, D., Gaudreault, N., Gerfen, C. R., Graddis, N., Groblewski, P. A., Henry, A. M., Ho, A., Howard, R., Knox, J. E., Kuan, L., Kuang, X., Lecoq, J., Lesnar, P., Li, Y., Luviano, J., McConoughey, S., Mortrud, M. T., Naeemi, M., Ng, L., Oh, S. W., Ouellette, B., Shen, E., Sorensen, S. A., Wakeman, W., Wang, Q., Wang, Y., Williford, A., Phillips, J. W., Jones, A. R., Koch, C. & Zeng, H. 2019. Hierarchical organization of cortical and thalamic connectivity. *Nature,* 575**,** 195-202.

Harris, K. D. & Shepherd, G. M. 2015. The neocortical circuit: themes and variations. *Nat Neurosci,* 18**,** 170-81.

Hazlett, H. C., Gu, H., Munsell, B. C., Kim, S. H., Styner, M., Wolff, J. J., Elison, J. T., Swanson, M. R., Zhu, H., Botteron, K. N., Collins, D. L., Constantino, J. N., Dager, S. R., Estes, A. M., Evans, A. C., Fonov, V. S., Gerig, G., Kostopoulos, P., McKinstry, R. C., Pandey, J., Paterson, S., Pruett, J. R., Schultz, R. T., Shaw, D. W., Zwaigenbaum, L., Piven, J., Network, I., Clinical, S., Data Coordinating, C., Image Processing, C. & Statistical, A. 2017. Early brain development in infants at high risk for autism spectrum disorder. *Nature,* 542**,** 348-351.

Heisenberg, C. P., Houart, C., Take-Uchi, M., Rauch, G. J., Young, N., Coutinho, P., Masai, I., Caneparo, L., Concha, M. L., Geisler, R., Dale, T. C., Wilson, S. W. & Stemple, D. L. 2001. A mutation in the Gsk3-binding domain of zebrafish Masterblind/Axin1 leads to a fate transformation of telencephalon and eyes to diencephalon. *Genes Dev,* 15**,** 1427-34.

Hentschke, H. & Stuttgen, M. C. 2011. Computation of measures of effect size for neuroscience data sets. *Eur J Neurosci,* 34**,** 1887-94.

Herculano-Houzel, S. 2009. The human brain in numbers: a linearly scaled-up primate brain. *Front Hum Neurosci,* 3**,** 31.

Hodge, R. D., Bakken, T. E., Miller, J. A., Smith, K. A., Barkan, E. R., Graybuck, L. T., Close, J. L., Long, B., Johansen, N., Penn, O., Yao, Z., Eggermont, J., Hollt, T., Levi, B. P., Shehata, S. I., Aevermann, B., Beller, A., Bertagnolli, D., Brouner, K., Casper, T., Cobbs, C., Dalley, R., Dee, N., Ding, S. L., Ellenbogen, R. G., Fong, O., Garren, E., Goldy, J., Gwinn, R. P., Hirschstein, D., Keene, C. D., Keshk, M., Ko, A. L., Lathia, K., Mahfouz, A., Maltzer, Z., McGraw, M., Nguyen, T. N., Nyhus, J., Ojemann, J. G., Oldre, A., Parry, S., Reynolds, S., Rimorin, C., Shapovalova, N. V., Somasundaram, S., Szafer, A., Thomsen, E. R., Tieu, M., Quon, G., Scheuermann, R. H., Yuste, R., Sunkin, S. M., Lelieveldt, B., Feng, D., Ng, L., Bernard, A., Hawrylycz, M., Phillips, J. W., Tasic, B., Zeng, H., Jones, A. R., Koch, C. & Lein, E. S. 2019. Conserved cell types with divergent features in human versus mouse cortex. *Nature,* 573**,** 61-68.

Huang, S. M., Mishina, Y. M., Liu, S., Cheung, A., Stegmeier, F., Michaud, G. A., Charlat, O., Wiellette, E., Zhang, Y., Wiessner, S., Hild, M., Shi, X., Wilson, C. J., Mickanin, C., Myer, V., Fazal, A., Tomlinson, R., Serluca, F., Shao, W., Cheng, H., Shultz, M., Rau, C., Schirle, M., Schlegl, J., Ghidelli, S., Fawell, S., Lu, C., Curtis, D., Kirschner, M. W., Lengauer, C., Finan, P. M., Tallarico, J. A., Bouwmeester, T., Porter, J. A., Bauer, A. & Cong, F. 2009. Tankyrase inhibition stabilizes axin and antagonizes Wnt signalling. *Nature,* 461**,** 614-20.

Iakoucheva, L. M., Muotri, A. R. & Sebat, J. 2019. Getting to the Cores of Autism. *Cell,* 178**,** 1287-1298.

Ji, X. Y., Zingg, B., Mesik, L., Xiao, Z., Zhang, L. I. & Tao, H. W. 2016. Thalamocortical Innervation Pattern in Mouse Auditory and Visual Cortex: Laminar and Cell-Type Specificity. *Cereb Cortex,* 26**,** 2612-25.

Kavaslar, G. N., Onengut, S., Derman, O., Kaya, A. & Tolun, A. 2000. The novel genetic disorder microhydranencephaly maps to chromosome 16p13.3-12.1. *Am J Hum Genet,* 66**,** 1705-9.

Kawaguchi, Y. & Kubota, Y. 1997. GABAergic cell subtypes and their synaptic connections in rat frontal cortex. *Cereb Cortex,* 7**,** 476-86.

Kazdoba, T. M., Leach, P. T., Yang, M., Silverman, J. L., Solomon, M. & Crawley, J. N. 2016. Translational Mouse Models of Autism: Advancing Toward Pharmacological Therapeutics. *Curr Top Behav Neurosci,* 28**,** 1-52.

Kim, S., Kim, H., Yim, Y. S., Ha, S., Atarashi, K., Tan, T. G., Longman, R. S., Honda, K., Littman, D. R., Choi, G. B. & Huh, J. R. 2017. Maternal gut bacteria promote neurodevelopmental abnormalities in mouse offspring. *Nature,* 549**,** 528-532.

Lewitus, E., Kelava, I., Kalinka, A. T., Tomancak, P. & Huttner, W. B. 2014. An adaptive threshold in mammalian neocortical evolution. *PLoS Biol,* 12**,** e1002000.

Lui, J. H., Hansen, D. V. & Kriegstein, A. R. 2011. Development and evolution of the human neocortex. *Cell,* 146**,** 18-36.

Lyngholm, D. & Sakata, S. 2019. Cre-Dependent Optogenetic Transgenic Mice Without Early Age-Related Hearing Loss. *Front Aging Neurosci,* 11**,** 29.

Marin, O. 2012. Interneuron dysfunction in psychiatric disorders. *Nat Rev Neurosci,* 13**,** 107-20.

Markram, H., Toledo-Rodriguez, M., Wang, Y., Gupta, A., Silberberg, G. & Wu, C. 2004. Interneurons of the neocortical inhibitory system. *Nat Rev Neurosci,* 5**,** 793-807.

Nelson, S. B. & Valakh, V. 2015. Excitatory/Inhibitory Balance and Circuit Homeostasis in Autism Spectrum Disorders. *Neuron,* 87**,** 684-98.

Nestler, E. J. & Hyman, S. E. 2010. Animal models of neuropsychiatric disorders. *Nat Neurosci,* 13**,** 1161-9.

Network, B. I. C. C. 2021. A multimodal cell census and atlas of the mammalian primary motor cortex. *Nature,* 598**,** 86-102.

O'Connor, K. 2012. Auditory processing in autism spectrum disorder: a review. *Neurosci Biobehav Rev,* 36**,** 836-54.

Olshausen, B. A. & Field, D. J. 2004. Sparse coding of sensory inputs. *Curr Opin Neurobiol,* 14**,** 481-7.

Piven, J., Arndt, S., Bailey, J., Havercamp, S., Andreasen, N. C. & Palmer, P. 1995. An MRI study of brain size in autism. *Am J Psychiatry,* 152**,** 1145-9.

Robertson, C. E. & Baron-Cohen, S. 2017. Sensory perception in autism. *Nat Rev Neurosci,* 18**,** 671-684.

Sakata, S. & Harris, K. D. 2009. Laminar structure of spontaneous and sensory-evoked population activity in auditory cortex. *Neuron,* 64**,** 404-18.

Sanchez-Marin, F. J. & Padilla-Medina, J. A. 2008. A Psychophysical Test of the Visual Pathway of Children with Autism. *Journal of Autism and Developmental Disorders,* 38**,** 1270-7.

Schmitzer-Torbert, N., Jackson, J., Henze, D., Harris, K. & Redish, A. D. 2005. Quantitative measures of cluster quality

for use in extracellular recordings. *Neuroscience,* 131**,** 1-11.

Senzai, Y., Fernandez-Ruiz, A. & Buzsaki, G. 2019. Layer-Specific Physiological Features and Interlaminar Interactions in the Primary Visual Cortex of the Mouse. *Neuron,* 101**,** 500-513 e5.

Shah, A. & Frith, U. 1983. An islet of ability in autistic children: a research note. *J Child Psychol Psychiatry,* 24**,** 613-20.

Shamash, P., Carandini, M., Harris, K. & Steinmetz, N. 2018. A tool for analyzing electrode tracks from slice histology. *bioRxiv,* 447995.

Silverman, J. L., Yang, M., Lord, C. & Crawley, J. N. 2010. Behavioural phenotyping assays for mouse models of autism. *Nat Rev Neurosci,* 11**,** 490-502.

Southwell, D. G., Paredes, M. F., Galvao, R. P., Jones, D. L., Froemke, R. C., Sebe, J. Y., Alfaro-Cervello, C., Tang, Y., Garcia-Verdugo, J. M., Rubenstein, J. L., Baraban, S. C. & Alvarez-Buylla, A. 2012. Intrinsically determined cell death of developing cortical interneurons. *Nature,* 491**,** 109-13.

Steinmetz, N. A., Zatka-Haas, P., Carandini, M. & Harris, K. D. 2019. Distributed coding of choice, action and engagement across the mouse brain. *Nature,* 576**,** 266-273.

Striedter, G. F. 1997. The telencephalon of tetrapods in evolution. *Brain Behav Evol,* 49**,** 179-213.

Szentagothai, J. 1983. The modular architectonic principle of neural centers. *Rev Physiol Biochem Pharmacol,* 98**,** 11-61.

Tang, X., Jaenisch, R. & Sur, M. 2021. The role of GABAergic signalling in neurodevelopmental disorders. *Nat Rev Neurosci,* 22**,** 290-307.

Thion, M. S., Mosser, C. A., Ferezou, I., Grisel, P., Baptista, S., Low, D., Ginhoux, F., Garel, S. & Audinat, E. 2019. Biphasic Impact of Prenatal Inflammation and Macrophage Depletion on the Wiring of Neocortical Inhibitory Circuits. *Cell Rep,* 28**,** 1119-1126 e4.

Verney, C., Takahashi, T., Bhide, P. G., Nowakowski, R. S. & Caviness, V. S., Jr. 2000. Independent controls for neocortical neuron production and histogenetic cell death. *Dev Neurosci,* 22**,** 125-38.

Williams, R. W. & Herrup, K. 1988. The control of neuron number. *Annu Rev Neurosci,* 11**,** 423-53.

Wilsch-Brauninger, M., Florio, M. & Huttner, W. B. 2016. Neocortex expansion in development and evolution - from cell biology to single genes. *Curr Opin Neurobiol,* 39**,** 122-32.

Wilson, H. R. & Cowan, J. D. 1972. Excitatory and inhibitory interactions in localized populations of model neurons. *Biophys J,* 12**,** 1-24.

Wong, F. K., Bercsenyi, K., Sreenivasan, V., Portales, A., Fernandez-Otero, M. & Marin, O. 2018. Pyramidal cell regulation of interneuron survival sculpts cortical networks. *Nature,* 557**,** 668-673.

Yague, J. G., Tsunematsu, T. & Sakata, S. 2017. Distinct Temporal Coordination of Spontaneous Population Activity between Basal Forebrain and Auditory Cortex. *Front Neural Circuits,* 11**,** 64.

Yao, Z., van Velthoven, C. T. J., Nguyen, T. N., Goldy, J., Sedeno-Cortes, A. E., Baftizadeh, F., Bertagnolli, D., Casper, T., Chiang, M., Crichton, K., Ding, S. L., Fong, O., Garren, E., Glandon, A., Gouwens, N. W., Gray, J., Graybuck, L. T., Hawrylycz, M. J., Hirschstein, D., Kroll, M., Lathia, K., Lee, C., Levi, B., McMillen, D., Mok, S., Pham, T., Ren, Q., Rimorin, C., Shapovalova, N., Sulc, J., Sunkin, S. M., Tieu, M., Torkelson, A., Tung, H., Ward, K., Dee, N., Smith, K. A., Tasic, B. & Zeng, H. 2021. A taxonomy of transcriptomic cell types across the isocortex and hippocampal formation. *Cell,* 184**,** 3222-3241 e26.

Ye, T., Fu, A. K. & Ip, N. Y. 2015. Emerging roles of Axin in cerebral cortical development. *Front Cell Neurosci,* 9**,** 217.

Supplementary Information

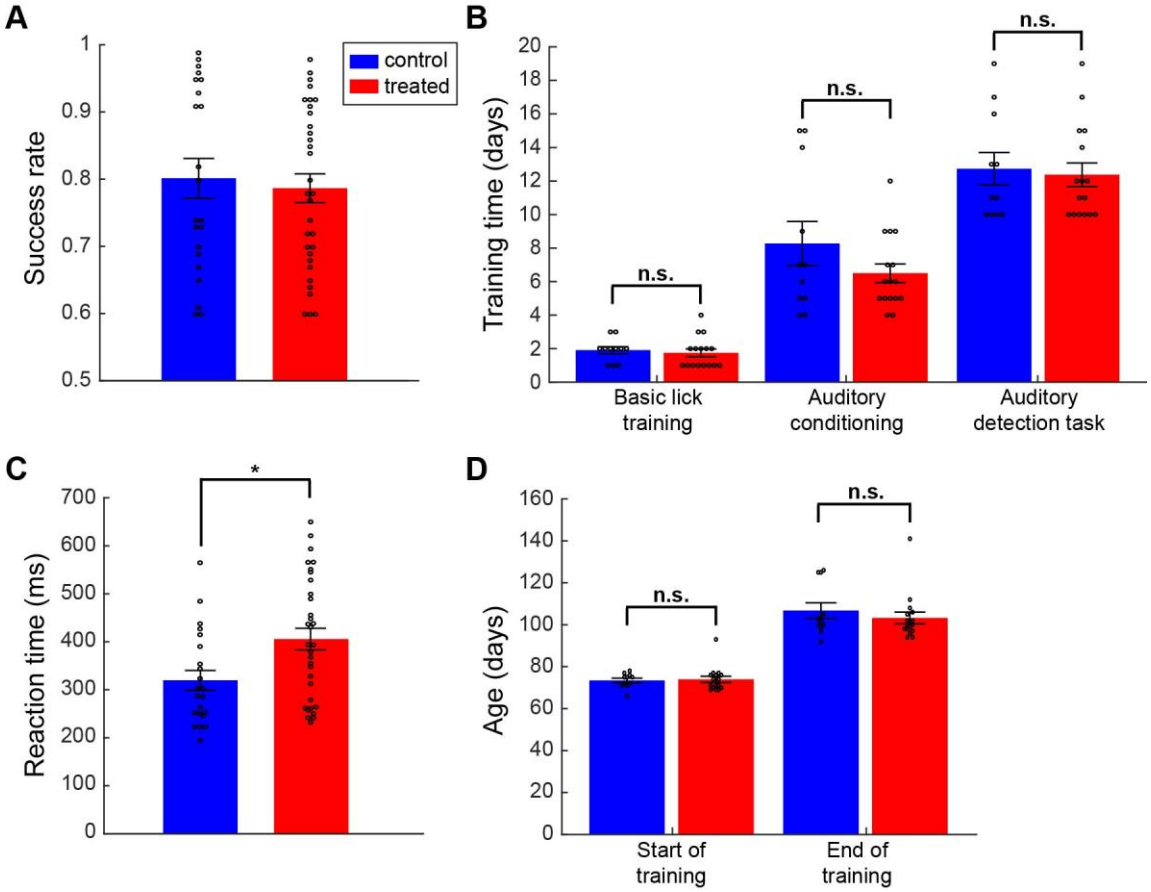

Figure 2 – Figure supplement 1 – Behavioral training progress and treatment effect in auditory conditioning.

(A) Success rate comparison in the last 2 sessions of auditory conditioning between treated and control groups (*n* = 22 vs. 32 sessions; 2 sessions per mouse). **(B)** Training time necessary for mice to pass each of the 3 phases in the behavioral assessment (*n* = 11 vs. 16 mice). **(C)** Comparison of reaction time between treatment groups in the last 2 sessions of auditory conditioning (*n* = 22 vs. 32 sessions; 2 sessions per mouse). **(D)** Age of the control and treated mice at the start and the end of behavioral assessment training (*n* = 11 vs. 16 mice). Error bars indicate SEM; *$p < 0.05$; *t*-test (**A – D**).

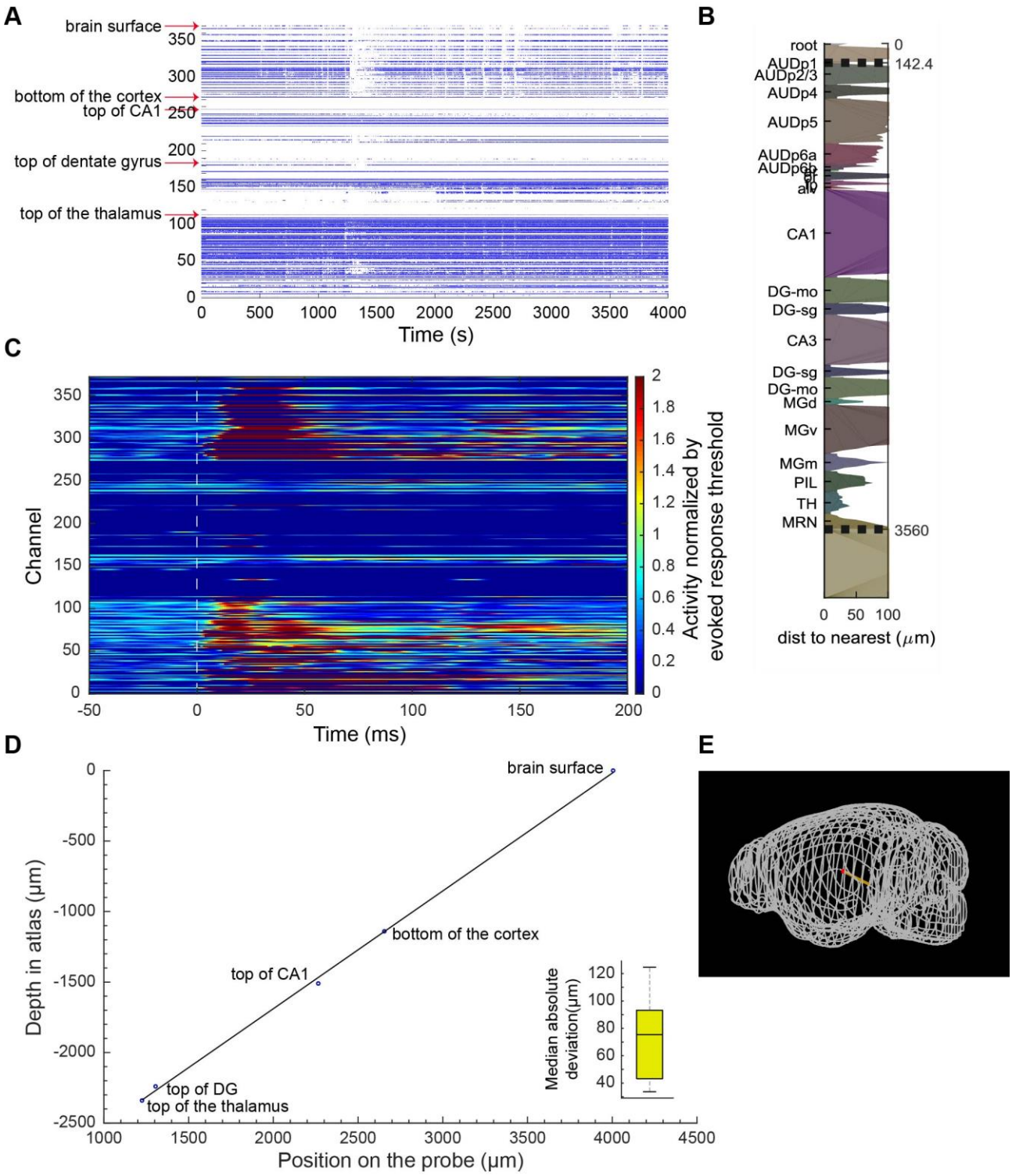

Figure 3 – Figure supplement 1 – Brain area estimation in Neuropixels recordings.
(A) Raster plot of activity across channels in time, for one recording. In each recording, five borders could be recognized (brain surface, bottom of the cortex, top of CA1, top of dentate gyrus and top of the thalamus). **(B)** SHARP-Track output profile with a list of brain areas caught by the probe. **(C)** Colormap of activity normalized by evoked response threshold across channels from one recording during 100 ms broadband white noise presentation (vertical white line marks the sound onset). Auditory evoked responses are visible in the cortex and thalamus (colors higher than 1 on the color bar). **(D)** Example of cross-validation procedure to assess alignment errors between histological and electrophysiological depth estimates. Linear regression analysis was used to assess the error for each brain area border (excluding that specific border in the computation). A median absolute deviation was then calculated for

each dataset, thus providing the range of alignment errors across all recordings (inset). **(E)** An example of a 3D mesh brain with the probe track location (orange line). Red dot indicates the brain surface.

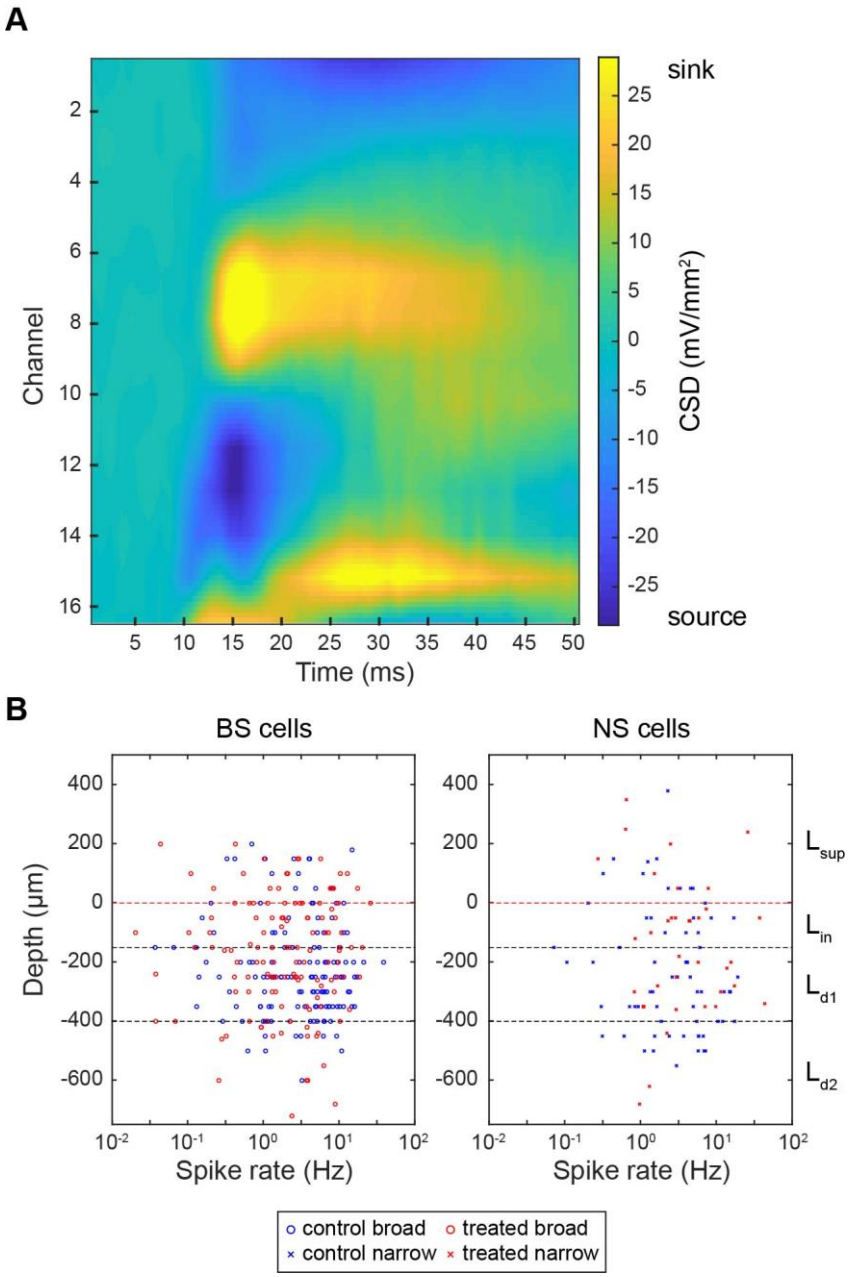

Figure 3 – Figure supplement 2 – Cortical cell depth determination with current source density. **(A)** Current source density (CSD) example for one shank (16 channels) of a silicon probe recording. Top current sink channel (yellow) is set as depth zero and the top border of input layer (L_{in}). Using CSD, neurons were divided into cortical layers depending on the depth of the channel with their largest amplitude of average spike waveforms. **(B)** Scatter plots of BS (left) and NS (right) neurons, showing their depth and cortical layer position as well as their spontaneous activity. Estimated layer borders are as follows: Superficial layers (L_{sup}) > 0 µm, input layer (L_{in}) 0 to -150 µm, deep layer 1 (L_{d1}) -150 to -400 µm, deep layer 2 (L_{d2}) < -400 µm.

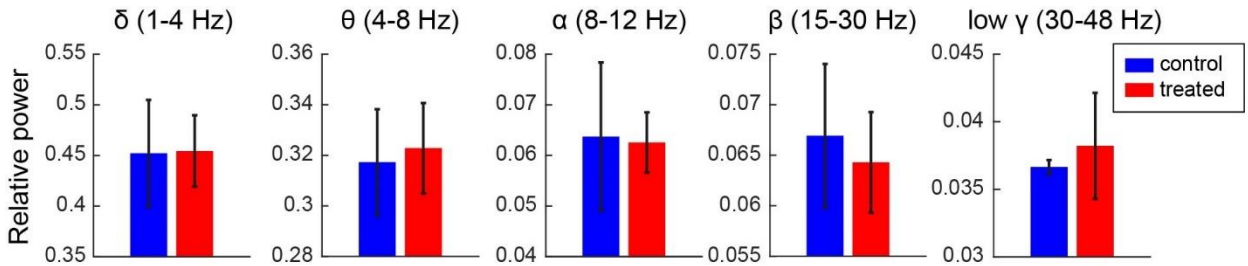

Figure 3 – Figure supplement 3 – Hippocampal relative power across frequency bands during silence. Comparison of mean relative power across hippocampal channels between control and treated mice, for each frequency band (*n* = 2 vs. 8 recordings). Error bars indicate SEM. None were statistically significant (*p* > 0.05; *t*-test).

A

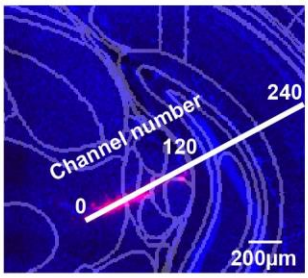

B

590 µm

upper border (µm)	lower border (µm)	area	
0	140	'AUDp1'	'Primary auditory area layer 1'
140	320	'AUDp2/3'	'Primary auditory area layer 2/3'
320	430	'AUDp4'	'Primary auditory area layer 4'
430	730	'AUDp5'	'Primary auditory area layer 5'
730	890	'AUDp6a'	'Primary auditory area layer 6a'
890	920	'AUDp6b'	'Primary auditory area layer 6b'
920	1000	'or'	'optic radiation'
1000	1080	'fp'	'corpus callosum posterior forceps'
1080	1100	'alv'	'alveus'
1100	1680	'CA1'	'Field CA1'
1680	1890	'DG-mo'	'Dentate gyrus molecular layer'
1890	1970	'DG-sg'	'Dentate gyrus granule cell layer'
1970	2350	'CA3'	'Field CA3'
2350	2390	'DG-sg'	'Dentate gyrus granule cell layer'
2390	2490	'DG-mo'	'Dentate gyrus molecular layer'
2490	2550	'fiber tracts'	'fiber tracts'
2550	2620	'TH'	'Thalamus'
2620	2900	'MGd'	'Medial geniculate complex dorsal part'
2900	2990	'MGv'	'Medial geniculate complex ventral part'
2990	3000	'MGm'	'Medial geniculate complex medial part'
3000	3210	'MGm'	'Medial geniculate complex medial part'
3210	3360	'PoT'	'Posterior triangular thalamic nucleus'
3360	3370	'POL'	'Posterior limiting nucleus of the thalamus'
3370	3380	'PoT'	'Posterior triangular thalamic nucleus'
3380	3510	'POL'	'Posterior limiting nucleus of the thalamus'

C

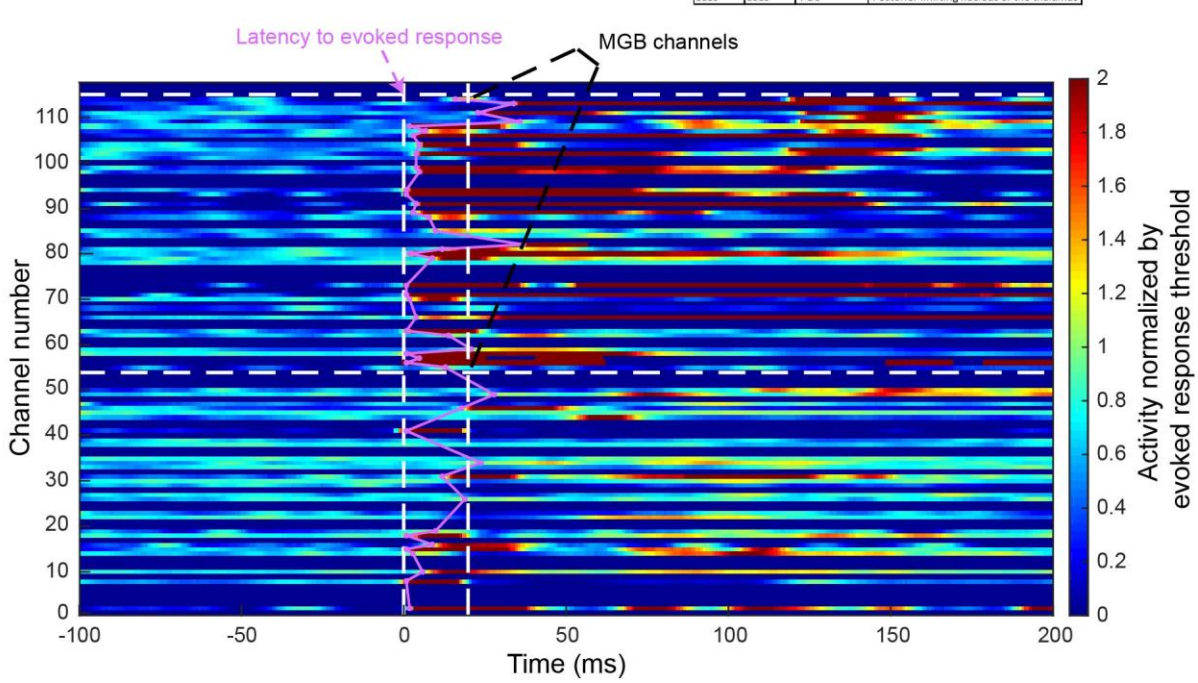

Figure 6 – Figure supplement 1 – Locating MGB in Neuropixels recordings.
(A) Schematics of a probe shank going through subcortical areas. Channel zero is located near the tip of the probe, and channel number is rising towards the cortex. **(B)** An example of a SHARP-Track output table showing the areas and their length caught by the probe. From this information, we calculated the approximate recorded length of MGB (590 µm), and converted this length into the number of channels (distance between channels is 20 µm and there are 2 rows of channels; therefore we expected 58 – 60 channels in MGB). **(C)** Colormap of activity normalized by evoked response threshold across subcortical channels from one recording (same as shown in **B**) during 100 ms broadband white noise presentation.

Starting from the tip of the probe (channel 0) and looking only at the subcortical channels, we determined the MGB channels based on the latency of evoked response (labelled in purple). Vertical white dashed lines indicate sound onset (0 ms) and 20 ms timepoint. By searching for a set of 58 – 60 channels with latency within 0-20 ms time window, we could refine the channel positions in MGB at the top of the thalamus (MGB borders marked with horizontal dashed lines).

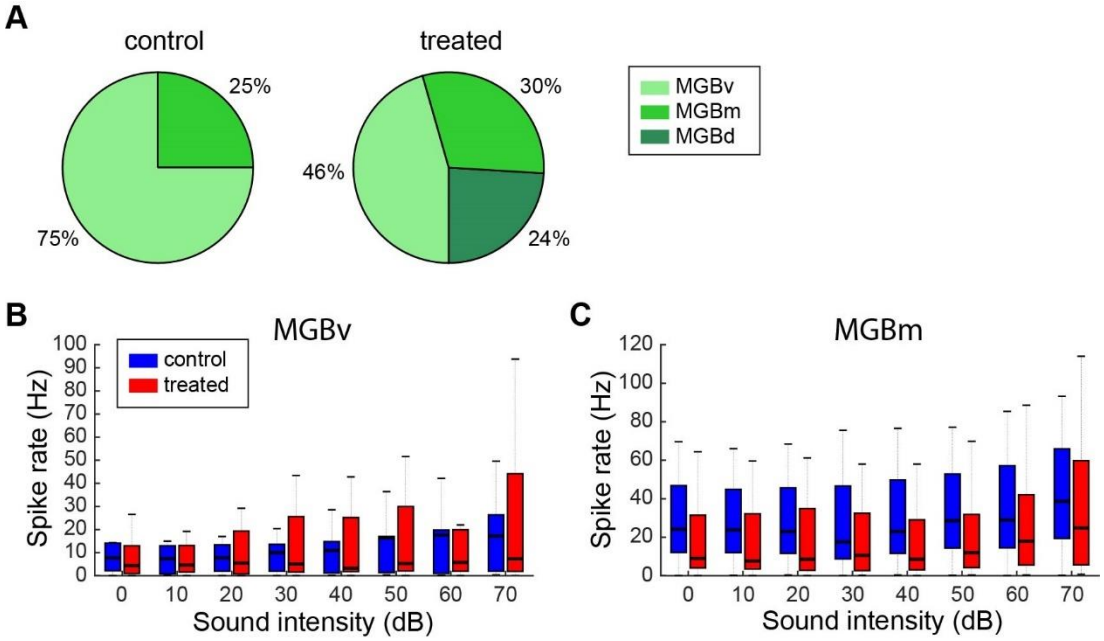

Figure 6 – Figure supplement 2 – Auditory evoked activity across MGB nuclei.
(A) Percentage of MGB neurons recorded across different nuclei in control (left) and treated (right) mice. In control, none of the MGB neurons were recorded from MGBd. **(B and C)** Spike rate comparison of MGBv **(B)** and MGBm **(C)** neurons in control and treated mice during the first 50 ms of sound presentation in passive listening conditions. None of the differences were statistically significant ($p > 0.05$; Rank sum test with Bonferroni correction) (**B** and **C**).